NOVA SCHOOL OF SCIENCE & TECHNOLOGY

DEPARTMENT OF ELECTRICAL AND COMPUTER ENGINEERING

SIMÃO AFONSO LOPES DE NORONHA PEREIRA DA COSTA

BSc in Electrical and Computing Engineering

MEASUREMENT OF AC LOSSES IN INDUCTIVE HTS FAULT CURRENT LIMITERS

MASTER IN ELECTRICAL AND COMPUTER ENGINEERING

NOVA University Lisbon

December, 2024

NOVA SCHOOL OF SCIENCE & TECHNOLOGY

DEPARTMENT OF ELECTRICAL AND COMPUTER ENGINEERING

MEASUREMENT OF AC LOSSES IN INDUCTIVE HTS FAULT CURRENT LIMITERS

SIMÃO AFONSO LOPES DE NORONHA PEREIRA DA COSTA

BSc in Electrical and Computing Engineering

Adviser: Prof. Doutor João Miguel Murta Pina
Associate Professor, Department of Electrical and Computer Engineering - NOVA School of Science and Technology

Co-adviser: Diogo Miguel Dias Durão
Synopsys Engineer

Examination Committee

Chair: Prof. Dr. Luís Filipe dos Santos Gomes
Associate Professor, Department of Electrical and Computer Engineering - NOVA School of Science and Technology

Rapporteur: Prof. Dr. Anabela Gonçalves Pronto
Associate Professor, Department of Electrical and Computer Engineering - NOVA School of Science and Technology

Adviser: Prof. Dr. João Miguel Murta Pina
Associate Professor, Department of Electrical and Computer Engineering - NOVA School of Science and Technology

MASTER IN ELECTRICAL AND COMPUTER ENGINEERING

NOVA University Lisbon
December, 2024

Measurement of AC losses in INDUCTIVE HTS FAULT CURRENT LIMITERS

This document was created with the (pdf/Xe/Lua)LaTeX processor and the NOVAthesis template (v7.1.10) [**novathesis-manual**].

A todos os que me apoiaram, nunca vos esquecerei.
Obrigado do fundo do coração.

Acknowledgements

A thousand words can not describe how grateful I am for all the help and support I had over these last few months. But I will try my best.

Firstly, I must thank Diogo Durão for all the hard work spent helping me and explaining to me in detail all the important processes, tasks, and experiments that allowed me to complete this thesis. I could not do this without you, thank you for your patience and dedication. When I was picking a thesis topic, I wanted an adviser that was as interested in the topic as I was; someone that showed me support and guidance but at the same time made me test my own limits. I am happy that I had Prof. João Murta Pina as my adviser, he provided me with all that and more with a charming personality. I feel like I became more independent thanks to him, it was a great honor.

This work would not be possible without the precious help and counseling of the Physics Department Instrumentation Lab technicians, Afonso Mountinho and Bruno Costa. Not excluding the many staff and students of the Electronics Department that gave me help in so many different ways. I would also like to thank the support of my friends for giving me strength and hope in the hardest of times in FCT, thank you for keeping me sane and healthy in these last months Tiago Lopes, Asdrúbal Noronha, Joaquim Lopes, and Carolina Azevedo.

Lastly, I want to thank my family and my friends up north for always caring for me and believing in me, despite all my flaws, they are always there for me when I need them. I am so grateful, thank you all so much!

Abstract

Power failures in high risk locations cause serious consequences in our day-to-day life. To ensure that this does not happen, it is essential to use instruments responsible for dealing with short circuits that inevitably occur, and thus, protecting equipment used in electrical energy distribution and transport. Their actions can save a lot of investments in fixings and replacements of many devices affected by short circuits.

Super-conducting Current Fault limiters (SFCLs) are commonly used to protect equipment in these networks, so it is important to be aware of the possible wear of the SFCL's so they may not affect the performance of other network equipment. They can be integrated into multiple locations in electrical grids, contributing to the electrification of the energy system, and taking an important role in Energy Transition.

Among the several kinds of SFCLs that have been developed, it is the Inductive Transformer-Type SFCL that will be the focus of this dissertation. It is comprised of a three-phase transformer with a short-circuited HTS winding as its secondary. By inducing voltage into these superconducting windings, AC losses are generated.

The purpose of this dissertation is to analyze the AC losses that affect the lifespan of Transformer-type SFCLs using a computer program developed in Python. By studying how the HTS windings will perform when integrated into SFCLs based on their characteristics, we can draw conclusions that will help enhance the production and design of HTS windings to reduce AC losses and improve the performance of SFCLs.

This objective was accomplished by creating three HTS windings from HTS tapes using methods for superconductor soldering and jointing, as well as developing multiple critical equipment for maintaining good system performance during operation. The SFCL in question is in normal operation (not when a short circuit occurs) and in Single-phase; the losses will be measured based on the instantaneous current and the electromotive force present on the HTS windings. Other experiments were made to test the methods of measuring the Solder Joint Resistance of the samples and their AC Losses when incorporated or not into the Inductive Transformer-type SFCL.

Keywords: Transformer-type SFCL, AC losses, HTS winding, Single-phase

Resumo

As falhas de energia em locais de risco causam graves consequências no nosso dia a dia. Para garantir que isso não aconteça, é fundamental a utilização de instrumentos responsáveis por lidar com os curtos-circuitos que inevitavelmente ocorrem e, assim, proteger os equipamentos utilizados na distribuição e transporte de energia elétrica. As suas ações podem economizar muitos investimentos em consertos e substituições de muitos dispositivos afetados por curtos-circuitos.

Os limitadores de corrente de curto-circuito supercondutores (SFCLs) são normalmente usados para proteger equipamentos nessas redes, daí a importância em observar qualitativamente os SFCLs para que estes não afetem o desempenho de outros elementos da rede. Podendo ser integrados em múltiplos locais das redes elétricas, contribuem para a eletrificação de sistemas energéticos, são assim importantes na Transição Energética.

Dos diversos tipos de SFCLs que foram desenvolvidos, é o SFCL do Tipo Transformador Indutivo que será o foco desta dissertação. É composto por um transformador trifásico com enrolamento HTS em curto-circuito como secundário. Ao induzir tensão nesses enrolamentos supercondutores, são geradas perdas AC.

O objetivo desta dissertação é analisar as perdas AC que afetam a vida útil de SFCLs do Tipo Transformador, utilizando um programa de computador desenvolvido em Python. Ao estudar o desempenho dos enrolamentos HTS quando integrados aos SFCLs, com base em suas características, podemos tirar conclusões que ajudarão a melhorar a produção e o projeto de enrolamentos HTS para reduzir as perdas AC e melhorar os seus desempenhos.

Este objetivo foi alcançado ao criar três enrolamentos HTS a partir de fitas HTS usando métodos para soldadura e união de supercondutores, bem como desenvolver vários equipamentos críticos para manter o bom desempenho do sistema durante a operação. O SFCL em questão está em operação normal (não quando ocorre curto-circuito) e em regime Monofásico; as perdas serão medidas com base na corrente instantânea e na força eletromotriz presente nos enrolamentos do HTS. Outras experiências foram realizadas para testar os métodos de medição da Resistência da junta de solda das amostras e as suas perdas AC quando incorporadas ou não no SFCL do tipo Transformador Indutivo.

Palavras-chave: SFCL tipo transformador, perdas AC, enrolamento HTS, monofásico

Contents

List of Figures viii

List of Tables xi

Acronyms xii

Symbols xiii

1 Introduction 1
- 1.1 Introduction of the HTS . . . 1
- 1.2 Objectives and Motivations . . . 2

2 State of Art 4
- 2.1 Superconductors . . . 4
  - 2.1.1 Type II or High Temperature Superconductors . . . 6
  - 2.1.2 AC Losses . . . 7
- 2.2 Fault Current Limiters . . . 8
  - 2.2.1 Transformer-Type Superconducting Fault Current Limiters . . . 8
- 2.3 Cryogenics . . . 10
- 2.4 Rogowski Coils . . . 11

3 Methodology and Project Setup 14
- 3.1 Method of Measuring AC Losses on the SFCL . . . 14
- 3.2 Method of Measuring Solder Joint Resistances in DC . . . 17
- 3.3 Method Proposed for Measuring the Electromotive Force . . . 18
- 3.4 Set up for the SFCL . . . 19
  - 3.4.1 Cryostats . . . 20
  - 3.4.2 Designing the Primary Windings . . . 22
  - 3.4.3 Creating a New Mold to fixate the Secondary Windings . . . 23
- 3.5 Set up for the System Devices . . . 24
  - 3.5.1 Production of HTS Tapes and Windings for the Secondary Windings 24

3.5.2 Cryostat instrumentation . . . 25
3.5.3 Creating a new holder for the HTS Tapes . . . 27
3.5.4 Electronic Circuits . . . 27
3.5.5 Data Processing . . . 30

4 Experiments and Discussions **32**
4.1 HTS Tapes Solder Joint Resistances in DC . . . 32
4.1.1 Results and Discussion . . . 32
4.1.2 No joint Experiment . . . 34
4.2 Tape AC Losses . . . 35
4.2.1 Sample E . . . 35
4.2.2 Sample G . . . 37
4.2.3 Sample H . . . 39
4.2.4 Discussion . . . 41
4.3 AC Winding Losses Using the SFCL (with iron core) . . . 42
4.3.1 Samples with bridge-type joints . . . 42
4.3.2 Samples with lap-type joints . . . 47
4.4 AC Experiments without using Iron Core . . . 55
4.4.1 Discussion . . . 62

5 Conclusion **63**

Bibliography **65**

Appendices

Annexes

I Annex **69**

List of Figures

2.1 Critical parameters of a superconductor. 5
2.2 Developing trend of superconducting critical temperature for conventional and cuprate superconductors over last 100 years. 7
2.3 Transformer type SFCL, with a load in single-phase circuit. 9
2.4 The applications of cryostats. 11
2.5 Rogowski coil with an RC integrator circuit. 12

3.1 Image of the iron cored SFCL alongside with one cryostat. 15
3.2 TPL5121 HTS tape layer configuration 15
3.3 Data diagram of all the devices present in an operational HTS winding for this experiment (on one leg of the transformer). 16
3.4 Diagram showcasing the method to measure the resistance of the HTS tapes 18
3.5 Experimental setup for the measuring AC losses of HTS winding samples. . 19
3.6 Diagram of the electric circuit equivalent to the setup. 20
3.7 Top and front views of the cryostat. 21
3.8 Cryostat lid and all its respective fittings. 22
3.9 Primary winding with 40 spirals. 23
3.10 Cast for holding the HTS winding during operation. 23
3.11 Types of joints. (a) lap joint. (b) bridge joint. 24
3.12 Image of one of the samples made. 25
3.13 Photo of HTS winding on its support with rogowski coil and soldered wires for voltage measurement. 26
3.14 Photos of cryostat lid with HTS winding connected. 26
3.15 Holder for the HTS tapes during operation. 27
3.16 Example of a schematic of circuit V. 28
3.17 Assembly used for calibrating the rogowski coils. 28
3.18 Orange rogowski coil with a small adhesive tape to keep it's shape. 29

4.1 Assembly for measuring the resistance of the created samples. 33
4.2 V-I curve of HTS tape joints. 33

4.3 Measured values of the no-joint sample. 34
4.4 Time graphs of electromotive force and current of sample E for the highest and lowest values of I_{AMP} 35
4.5 Graph of calculated average energies for single-phase sample E and respective power law fit curve in relation to current amplitude 36
4.6 Graph of calculated average Resistance for single-phase sample E and respective linear fit curve in relation to current amplitude 36
4.7 Time graphs of electromotive force and current of sample G for the highest and lowest values of I_{AMP} 37
4.8 Graph of calculated average energies of sample G and respective power law fit curve in relation to current amplitude 38
4.9 Graph of calculated average resistance values of sample G and respective linear fit curve in relation to current amplitude 38
4.10 Time graphs of electromotive force and current of sample H for the highest and lowest values of I_{AMP}. 39
4.11 Graph of calculated average energies for single-phase sample H and respective power law fit curve in relation to current amplitude 40
4.12 Graph of calculated average Resistance for single-phase sample H and respective linear fit curve in relation to current amplitude 40
4.13 Assembly of all equipments for the measuring the ac losses of the bridge-type windings. 42
4.14 Time graph of electromotive force and current of sample I for the highest values of I_{AMP} 43
4.15 Graph of calculated average energies for single-phase sample I and respective power law fit curve in relation to current amplitude 44
4.16 Time graph of electromotive force and current of sample J for the highest values of I_{AMP} 45
4.17 Graph of calculated average energies for single-phase sample J and respective power law fit curve in relation to current amplitude 45
4.18 Assembly of all equipments for measuring the ac losses of the lap-type windings. 47
4.19 Time graph of electromotive force and current of sample 1 for the highest values of I_{AMP}. 48
4.20 Graph of calculated average energies for single-phase sample 1 and respective power law fit curve in relation to current amplitude; when using a 40 spiral primary 49
4.21 Graph of calculated average energies for single-phase sample 1 and respective power law fit curve in relation to current amplitude; when using a 10 spiral primary 49
4.22 Time graph of electromotive force and current of sample 2 for the highest values of I_{AMP}. 50

4.23 Graph of calculated average energies for single-phase sample 2 and respective power law fit curve in relation to current amplitude; when using a 40 spiral primary . . . 51
4.24 Graph of calculated average energies for single-phase sample 2 and respective power law fit curve in relation to current amplitude; when using a 10 spiral primary . . . 51
4.25 Time graph of electromotive force and current of sample 3 for the highest and lowest values of I_{AMP}. . . . 52
4.26 Graph of calculated average energies for single-phase sample 3 and respective power law fit curve in relation to current amplitude; when using a 40 spiral primary . . . 53
4.27 Graph of calculated average energies for single-phase sample 3 and respective power law fit curve in relation to current amplitude; when using a 10 spiral primary . . . 53
4.28 Assembly of the samples when not using the iron core of the SFCL. . . . 55
4.29 Time graph of electromotive force and current of sample 1 for the highest values of I_{AMP} and for a distance of 12cm. . . . 56
4.30 Time graph of electromotive force and current of sample 1 for the highest values of I_{AMP} and for a distance of 6cm. . . . 56
4.31 Graph of calculated average energies for single-phase sample 1 and respective power law fit curve in relation to current amplitude . . . 57
4.32 Time graph of electromotive force and current of sample 2 for the highest values of I_{AMP} and for a distance of 12cm. . . . 58
4.33 Time graph of electromotive force and current of sample 2 for the highest values of I_{AMP} and for a distance of 6cm. . . . 58
4.34 Graph of calculated average energies for single-phase sample 2 and respective power law fit curve in relation to current amplitude . . . 59
4.35 Time graph of electromotive force and current of sample 3 for the highest values of I_{AMP} and for a distance of 12cm. . . . 60
4.36 Time graph of electromotive force and current of sample 3 for the highest values of I_{AMP} and for a distance of 6cm. . . . 60
4.37 Graph of calculated average energies for single-phase sample 3 and respective power law fit curve in relation to current amplitude. . . . 61

I.1 Schematic of the mold used for the winding samples. . . . 70

List of Tables

4.1 AC power losses and resistance values of each sample. 41
4.2 AC power losses of each sample, for windings with bridge-type joints. . . . 46
4.3 AC losses of each samples depending on the number of spirals of the primary. 54
4.4 AC power losses of each sample, without using the iron core. 62
4.5 Registered AC losses of all the samples, for all experiments made. 62

Acronyms

AC Alternating Current *(pp. 2, 9, 11, 13, 15, 17, 24, 28, 29, 63, 64)*

CSV Comma-separated Values *(pp. 17, 30)*

DC Direct Current *(pp. 9, 17, 18, 30, 37, 63)*

FCL Fault Current Limiter *(p. 8)*

HTS High Temperature Superconductor *(pp. viii, 1–3, 5–9, 15–18, 20, 23–29, 32, 34, 63, 64)*

LN2 Liquid nitrogen *(pp. 1, 2, 14, 18, 27)*

LTS Low Temperature Superconductor *(pp. 2, 5)*

NRMSE Normalized root mean squared error *(pp. 32, 36, 37, 39, 43, 44, 46, 48, 50, 52, 54, 57, 59, 61, 62)*

PLA Polylactic Acid *(pp. 23, 63)*

SC Superconductor *(pp. 2, 7, 14)*

SFCL Superconductor Fault Current Limiter *(pp. viii, 1–3, 8, 9, 14, 15, 63, 64)*

SFCLs Superconductor Fault Current Limiters *(pp. 1, 3, 8, 64)*

SQL Structured Query Language *(pp. 2, 35, 37, 39, 43, 44, 47, 50, 52, 55, 57, 59)*

YBCO Yttrium barium copper oxide *(pp. 1, 8)*

Symbols

α	Power function coefficient *(pp. 32, 41, 54)*
B	Magnetic flux density *(pp. 5, 6)*
β	Power function exponent *(pp. 32, 43, 62)*
d	Perimeter of the Winding *(p. 16)*
ϵ	Electromotive force *(pp. 30–32, 35, 37, 39, 43, 44, 48, 50, 52, 56, 57, 59, 64)*
H	Applied magnetic field *(pp. 5, 6)*
H_c	Critical Magnetic field of Superconductor *(p. 5)*
H_{c1}	Lower critical field *(p. 6)*
H_{c2}	Higher critical field *(p. 6)*
i	Instantaneous current *(pp. 12, 16, 30–32, 35, 37, 39, 43, 44, 48, 50, 52, 57, 59, 61)*
I_{AMP}	Current amplitude *(pp. ix, x, 31, 35, 37, 39, 43–45, 47, 48, 50, 52, 54–60)*
J	Electric current density *(p. 4)*
J_c	Critical current density *(p. 5)*
l	Smallest winding loop arc distance between two points *(p. 16)*
M	Magnetization *(p. 5)*
Q	Average power dissipated (in mJ/cycle) *(p. 32)*
ρ	Electrical Resistivity of a Material *(p. 4)*
R_{solder}	Solder joint resistance *(pp. 17, 32, 34, 41, 54)*

T_c	Critical Temperature of Superconductor *(pp. 4–6)*
u	Instantaneous voltage *(p. 12)*
U_{rog}	Amplified and integrated u_{rog} *(p. 27)*
u_{rog}	Output voltage from Rogowski *(pp. xiv, 17)*
u_v	Voltage between two points of the HTS winding *(pp. 55, 57, 59)*

1 Introduction

Electrical energy consumption is rapidly growing in order to keep up with the power needs in all the different sectors of our population [1], so it is vital that electrical networks can safely and consistently supply electricity to each consumer on the network. A big priority in power grids and any type of power systems is the prevention of short circuits, as they can have devastating impacts.

The most common way for power systems to protect their circuits from over-currents is with the use of circuit breakers, however, they are subject to irreparable damage whenever there is a fault, and so there may come a time when they are incapable of interrupting a short circuit. Instead of replacing the equipment or building a new substation in parallel, another cheaper solution to dealing with the faults is the use of Superconducting Fault Current Limiters or SFCLs,[2], a device that swiftly limits the current whenever a short-circuit occurs. Due to their characteristics, they present low nominal losses when the system is operating in an normal regime and provide a direct response, without requiring the intervention of other mechanisms, and also have a quick reaction time [3].

To limit the fault currents it is necessary to increase the line transmission impedance, for that the SFCLs, with the use of high temperature superconductive windings (HTS windings), will act and apply a resistive or an inductive impedance connected in series with the transmission line as soon as the fault current is detected.

1.1 Introduction of the HTS

The SFCL in question is composed of a three-phase transformer whose secondary windings are made of High Temperature Superconductors (HTS's) tapes and short-circuited; more specifically YBCO tapes.

In order for the HTS's tapes can reach their superconductivity, they have to be submitted to an average operation temperature lower than their critical temperature, to achieve this, it is required the use of cryostats. In this case, the cryostat that we are using holds Liquid Nitrogen (LN2) as a cooling agent, which results in operating temperatures of around 77 degrees Kelvin.

Under constant current operations, the superconductors carry electricity while providing no resistance, so there are no losses. But with AC current some of them are generated, thanks to the inducted currents that operate in the normal conducting regions of these SC.

These losses inevitably lead to temperature rises inside of the superconductors, resulting in the evaporation of the surrounding nitrogen. Therefore, the cryostat, that has to contain a steady quantity of LN2 levels to the SC's during operation. By studying and measuring these energy losses, we gain a better understanding of the power behavior at hand and reach conclusions about the best possible solutions and devices that may help to improve them.

The study of HTS based systems, specifically when it comes to their behavior and design implementations, prove to be a very relevant topic and one that can positively impact important sectors of our society, for example, improving naval structures [4] and power cables [5].

Since we are dealing with HTS, their critical temperature is significantly higher comparing to Low Temperature Superconductor (LTS) (below 23 K). Liquid nitrogen is an alternative to the previously used cooling agent, liquid helium. That's because it's effective for maintaining the desirable temperatures of around 77 K it is also considerably less volatile and expensive in comparison to liquid helium [6].

1.2 Objectives and Motivations

This dissertation will focus on studying the AC energy losses of an inductive transformer type SFCL, in order to find out how we can improve design and production of HTS windings to reduce these losses and thus helping transformer to prevent short circuits more efficiently. It also studies its behavior and the effects that may provoke on other devices when those losses emerge.

The aim is to measure them when they are caused by balanced system losses, which means calculating the electromotive force induction present in the secondary HTS windings of the SFCL. This will be made possible through the use of a python program that is capable measure these losses by processing relevant data obtained by the system. The program would be designed by receiving Structured Query Language (SQL) type files containing the various output signals of the system, that are read by the oscilloscopes. It then analyses and processes the output signals and then calculates measured losses.

This dissertation engages the same objectives of a dissertation published by Diogo Durão, a previously Physics Engineering student in NOVA School of Science and Technology. However it aims to recreate the same results but reach different conclusions based on the production methods of creating HTS samples that are able to be incorporated into a Transformer-type SFCL. Since most equipments that will be used were already designed by Diogo, with his guidance, notice that most topics at hand were already explored both in his dissertation [7] and in the article [8] also written by him.

The SFCL that we're studying consists of a three-phase transformer with three short-circuited HTS windings, with a closed iron core since it presents more advantages than with an open one. For example, with an open-core, the magnetic field generated in a large space outside the limiter leads to the decrease of the quenching time and it can disturb the operation of nearby devices [9].

SFCLs are still a popular subject of many studies, thanks to their unique characteristics and practical applications. So if we could learn potential improvements of their usages or gain a better knowledge of their behaviors, it could bring significant advantages when it comes to efficiency, cost savings and easier maintenance of equipments in electrical grids. This dissertation aims to do exactly that, and it may hopefully be used to help further studies that involve the use of SFCLs.

The remainder of this dissertation is composed by four more chapters:

- **State of Art**, that contains all of the essential theoretical concepts needed to understand what is to be studied.
- **Methodology and Project Setup** It presents the methods for acquiring the power losses and describes the equipment used and the various tasks involved in creating and calibrating a variety of practical instruments for the system setup.
- **Experiments and Discussions** Contains the description of the conducted experiments, a summary of the results and a brief discussion that delves into the meaning and relevance of said results.
- **Conclusion** This section summarizes the research findings, outlines the limitations of the project and also provides a recommendation for future research.

2

State of Art

In order for this project to be successful and reach its goal, there needs to be a good understanding of the previously mentioned topics. This chapter will cover all necessary the theoretical concepts needed to make sure the system is well designed and to know it will behave accordingly to our expectations.

2.1 Superconductors

The phenomenon of superconductivity was first discovered in 1911, by H. Kamerlingh-Onnes, during a study to discover how the properties of various metallic materials change when subjected to very low temperatures, with the use of cryogenics. Back then, there was only the knowledge that the electrical resistance of metals decreased with temperature. Still, Onnes found out that, the resistance of a mercury wire dropped very abruptly at about 4 degrees kelvin, until completely vanishing.

To differentiate the "normal metals" from the ones with these properties, this new state of the material was dubbed as a superconducting state; meaning that if a conductive material is below a given critical temperature, T_c, it exhibits a virtually zero resistivity; conducting electricity without any losses.

To verify the absence of resistance, a measurement of the electrical current density of the material was carried out. The following equation 2.1 is used, as the electric current density, J, will remain equal to the initial value attributed over time, whenever its resistance value is null, (which means the resistivity, ρ, is null).

$$\rho = \frac{E}{J} \tag{2.1}$$

In 1933, Walter Meissner and Robert Ochsenfeld discovered that there was also an absence of magnetic fields within the superconducting metals, meaning that they expel magnetic fields from their interior while in a superconducting state. This means the discovery of another property of the superconducting materials, as they also are perfect diamagnets. This characteristic distinguishes a superconducting material from perfect conductors. This phenomenon remains known as the Meissner effect, and as long as the applied

magnetic field does not exceed a certain critical value, H_c, the magnetic induction inside the superconductor is null.

The superconductors will have a flux density, B, represented by following equation:

$$\overrightarrow{B} = \mu_0(\overrightarrow{H} + \overrightarrow{M}) \tag{2.2}$$

which will be null ($B = 0$), as long as the applied magnetic field doesn't reach critical values H_c. This means that the magnetization has the same modulus and opposite direction to that of the applied field ($M = -H$) , expelling the magnetic flux, just as perfect diamagnets act.

The reasoning behind the superconductivity phenomenon was theoretically explained by John Bardeen, Leon Cooper, and Robert Schrieffer in 1957. This theory is based on the concept of electron pairing, which is caused by interactions or coupling between electrons and vibrations of the crystal lattice of the material, they then create a weak attraction that can lead to the formation of electron pairs called cooper pairs. They are defined as a correlated state of two conduction electrons with no net kinetic linear momentum and zero net spin. Due to the quantization of the angular momentum of the cooper pairs and the formation of a macroscopic quantum state (thanks to their behavior), superconducting materials provide zero heat, resistance, and induction [10].

The following Figure 2.1, modified from [11], best illustrates the schematic diagram of the many critical parameters of a superconductor, T_c, J_c, and H_c. For both High and Low Temperature Superconductors (HTS and LTS).

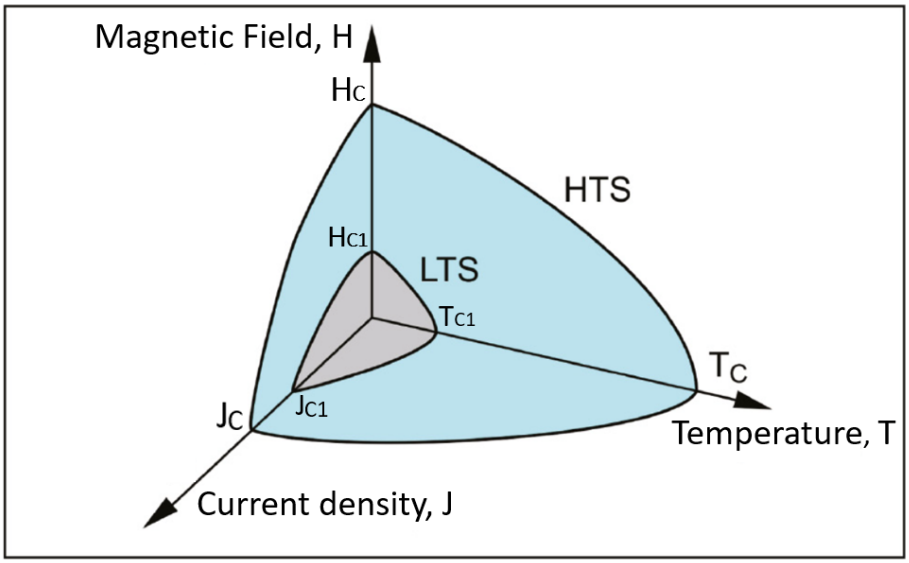

Figure 2.1: Critical parameters of a superconductor.

2.1.1 Type II or High Temperature Superconductors

There are two types of superconductors: types I and II; with the biggest difference between them is the fact that, unlike the type I superconductors that only reach one superconducting state called the Meissner state, type II superconductors reach an extra intermediate state, where the magnetic flux pierces the material, but without it losing superconductivity.

Type II superconductors allow magnetic flux penetration inside the metal, as they act in a new state called the Mixed state. The flux starts penetrating at a lower critical field than the type I materials, H_{c1}, but reaches B=H at a higher critical field H_{c2}. H_{c2} can be much greater than H_{c1} thanks to the energy cost that is preventing the field from going inside of the superconductor [12].

These unique properties allow type II superconductors to have a more practical use rather than type I. Some of the key differences are:

- **Higher Critical Magnetic Fields** Thanks to their higher range of critical magnetic fields, type II superconductors are more capable of maintaining their superconductivity in higher magnetic fields, making them more suitable for applications where superconductors are subjected to strong fields, like when used in power grids and transmission lines.

- **Practical Temperature Range** Most type II superconductors have a higher critical temperature, T_c, than Type I. This property makes them more capable of operating at higher ranges of temperatures and also operate with other alternatives for cooling agents, rather than unsafe and expensive options like liquid helium.

In 1986 high-temperature superconductors, were first discovered by J. G. Bednorz and K. A. Müller. These superconductors, capable of achieving critical temperatures of 30 K and above in ceramic compounds, marked a significant advancement in the field and are commonly referred to as HTS.

To achieve high values of T_c, it is necessary a powerful electron-lattice attraction, and with further studies these scientists discovered that the most suitable materials were the ceramic cuprates thanks to their unique characteristics that allow the materials to reach the superconducting state at higher transition temperatures [13]. The development of ceramic cuprates evolved throughout the years, which led to the discovery of superconducting materials with a T_c that reached values beyond 130 K. This allowed the use of liquid nitrogen (77 K boiling point) as a cooling agent; a great achievement since the aforesaid is safer, cheaper, and easier to obtain than the use of liquid helium (4 K boiling point).

Figure 2.2, from [11], displays the evolution of T_c for various conventional and high-temperature superconductors, and their respective year of discovery. The compounds whose scientific names are written in red belong to cuprates while the names in blue and green belong to the groups of intermetallics and iron-based superconductors, respectively.

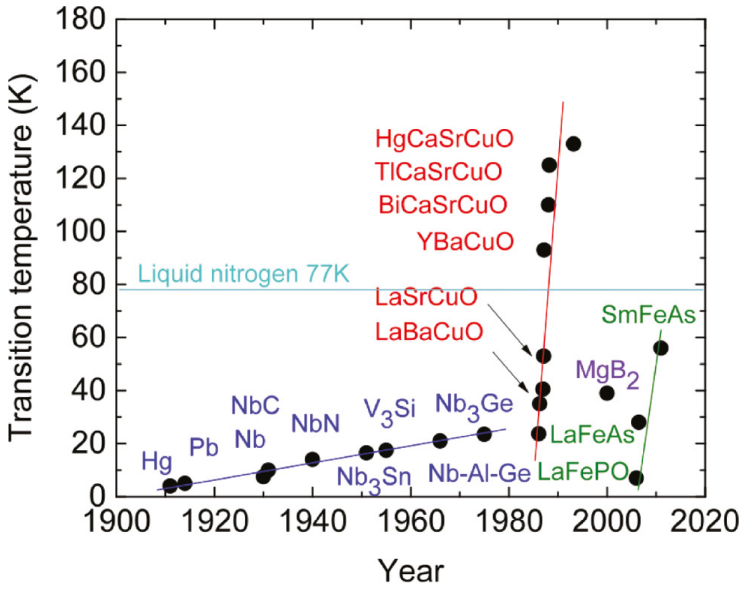

Figure 2.2: Developing trend of superconducting critical temperature for conventional and cuprate superconductors over last 100 years.

These studies helped the discovery of many great applications of cuprate HTS's in multiple fields; which include areas like Electronics, Power Engineering, Medical Technologies, and Basic Research [14].

2.1.2 AC Losses

Ideally, the magnetic flux crossing through a superconducting material is null thanks to the meissner effect (the magnetic field of the superconductor is always symmetrical to the applied magnetic field). Therefore, in accordance to the differential form Ampere's Law ($\nabla \times E = -dB/dt$), no electric field would be created and there would be no dissipation of energy.

However, that is not the case when dealing with AC currents in High Temperature superconductors, as they create electric fields parallel to the current, and therefore, there is always energy losses via power dissipation. The alternating magnetic fields also produce energy losses in superconductors, this is because the magnetic field that penetrates the material is constantly changing and, when pinned by defects or imperfections in the superconducting structure, the flux-line pattern and internal magnetic field change as well, generating power losses. These magnetization losses are the type of AC Losses that happen in this type of project.

Other types of losses that can occur when a SC is subjected to a time-varying magnetic field are Eddy current losses. They occur when the magnetic field penetrates into a normal conductor or in the metal matrix [15], and induces an electric field that makes currents flow.

In addition to these losses, it's important to note that any joint in a superconducting circuit adds resistance to the system, which can lead to significant AC losses whenever

high currents pass through the joint.

2.2 Fault Current Limiters

As it was previously mentioned in the Introduction at the beginning of chapter 1, although circuit breakers and switch gears with high cutting power can, on their own, stop a short circuit current from spreading; these devices suffer damages that, if prolonged, can lead them disabled or even fully destructed.

Therefore, it is common the use of current transformers as they are capable of enduring high currents and limiting them, until those aforementioned devices with cutting power act, to protect the power system from further damages that they may cause. For that, it is necessary to use devices that start with a small impedance at nominal operation but with the ability to swiftly increase their impedance at fault conditions.

Fault Current Limiters (FCL) grant security and stability to power systems, along with many other benefits to electric utilities [16]. There are various types of FCL with many distinct features, which can classified in several ways:

- **Resistive vs Inductive FCLs**, where these differ based on the use of high amounts of resistance or induction to increase the impedance necessary for limiting the fault current.
- **Superconducting vs Non-Superconducting FCLs**, based on whether or not superconducting materials are utilized.
- **Shielded vs Iron-Cored FCLs**, where shielded FCL use magnetic shielding to influence magnetic flux and manage current flow, minimizing electromagnetic interference that can be delivered to sensitive equipment. In contrast to iron-cored FCL to handle higher magnetic flux densities, allowing them to withstand repeated fault conditions without significant wear.

2.2.1 Transformer-Type Superconducting Fault Current Limiters

Since high temperature superconductors are capable of withstanding high current densities (upwards of $10^4 \mathrm{A/mm}^{-2}$, for YBCO tapes) with zero impedance, making them natural current fault limiters. When subjected to a high enough current while in a superconducting state, they change to a normal state becoming a resistive material (thanks to their ceramic properties) and thus limiting the current. Once the fault is dealt with they return to their superconducting state. This change of state phenomenon is also called a quench.

SFCLs have many applications in different parts of the power network such as renewable power and distribution generation [17], transmission systems [18] and distribution networks [19].

Therefore it's advantageous to combine both of them into one SFCL, in this dissertation focuses on one particular type of HTS Fault Current Limiter called a transformer Type SFCL.

They are composed of two sides, a primary side of the transformer, that is connected in series with the load and a secondary side that is connected in series with superconducting windings [20], instead of the normal copper ones in the primary side.

Figure 2.3, modified from [20], illustrates the electric circuit of a transformer Type SFCL and its various components. In this figure, the symbols L1 and L2 represent the induction present in the primary and secondary sides of the transformer, respectively; with M representing the mutual inductance between both of them.

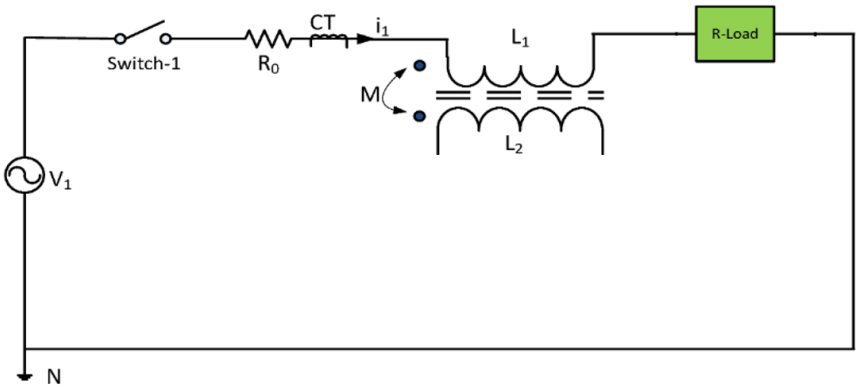

Figure 2.3: Transformer type SFCL, with a load in single-phase circuit.

The superconductors present in the secondary side magnetically shield the iron core, which makes the devices impedance negligible in nominal operation.

Every time a fault occurs, the superconductors in the secondary side of the transformer quenches (transitions from its superconducting state to its normal state), and consequently limits the current in the secondary side to a lower value. However, the core can no longer balance the magnetic flux produced by the primary side, therefore it starts to reduce those flux quantities, by increasing the induction coefficient, until the current flowing in primary side is limited as well.

It is also important to point out that AC losses are generated by the electromotive force in the HTS windings. Other examples of SFCL are:

- **Bridge type SFCL**

  The SFCL consists of superconducting branches arranged in a bridge structure and connected in parallel to the power system. This configuration allows for a controlled and gradual limitation of fault currents by distributing the fault current across multiple branches, offering advantages over other configurations.

- **Saturated-cores type SFCL**

  From where the nonlinear impedance characteristic required to limit the short-circuit currents is obtained by connecting two iron core coils. Both are driven into saturation by the DC introducing DC bias currents which cause the magnetic flux of the circuits to operate around the DC bias magnetic fields [21].

- **Resistive type SFCL**

  It consists of a superconducting component and a resistance connected in parallel to the grid. The resistive element is not present during normal system operation, allowing the superconductor to carry the current without resistance. But when a short-circuit occurs it then connects, affecting the rest of the circuit by actively limiting the fault current by introducing a resistance increase.

2.3 Cryogenics

Cryogenics is the science, that deals with the study of processes and material properties that are subjected to very low temperatures, generally below 120 K. These studies intend to better understand what effects and behaviors, from these processes and materials, are to be expected and specially how we can take the most benefit out of them.

The first experiments ever conducted were with the use of compressed gas refrigerators invented by James Harrison in 1856. Not so long after, new inventions started to arrive like the vacuum flask and liquefied air, but the most relevant one was probably the emergence of new cryogenic technologies that were granted by the liquefaction of materials that became popular cooling agents for the years to come. For example:

- **Carbon Dioxide**, between 1823 and 1845 by Michael Faraday.
- **Oxigen and Nitrogen** in 1877 by Raoul Pictet and Louis Paul Cailletet.
- **Hydrogen** in 1898, by James Dewar.
- **Helium** in 1908, by H. Kamerlingh-Onnes, the father of superconductivity.

By applying extremely low temperatures on materials such as metals, alloys and other composites alike, some particular qualities can be enhanced to make them more effective in whatever application that those materials might be used on. In regards to superconducting materials, for a well defined range of temperatures, it refines and stabilizes the crystal lattice structure of the materials, thus allowing the existence of cooper pairs that are responsible for superconductivity. Also, to hardened steels and similar alloys, cryogenic processing can distribute carbon particles throughout the materials turning them stronger and hence more durable (to quote [22]).

The cryostat is a device designed specifically for maintaining a constant cryogenic temperature. The term comes from the Greek word "cryo," meaning cold, and the word "stat," which translates to stable. This device is a container for liquefied gases and is capable of regulating the quantities that are to be expelled. The first cryostat was invented by Sir James Dewar, who called it a vacuum flask. This silver-plated, double-walled container with a vacuum between the walls was initially used to collect the first liquefied hydrogen in 1898. This invention greatly improved the thermal insulation of liquids and

is still widely used today due to its many applications, as shown in Figure 2.4, taken from [23].

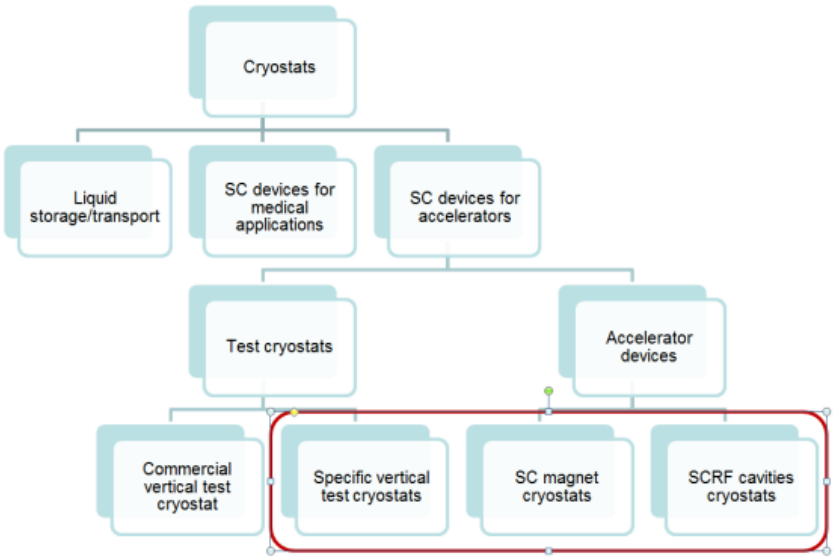

Figure 2.4: The applications of cryostats.

As stated before, the fundamental objective of a cryostat is to house and thermally insulate a superconducting device, but at the same time provide communication between different components in the system while guaranteeing reliability and safety throughout the operation. Therefore it is vital that some technical requirements are met when designing a cryostat, in regards to mechanical engineering and heat transfer processes. However, the instruments and behaviors of the cryostat can become quite hard to achieve at very low temperatures, as there is a need to pay great attention to the properties of the materials.

These requirements can only be achieved by a system integration of complex devices to be enclosed inside the insulation vacuum and capable of enduring cryogenic temperatures[23], such as cryogenic instrumentation, Beam Position Monitors (BPM), electrical circuits, and control devices.

2.4 Rogowski Coils

Rogowski coils are a type of electrical device commonly used to measure AC and transient currents. More specifically it is an air-core coil with toroidal form windings, invented by German physician Walter Rogowski for the purpose of measuring the values of currents flowing in electrical conductors. It is not composed of a ferromagnetic core, meaning that it has a linear characteristic.

With the technical advancements throughout the years, the Rogowski Coil cost of fabric has dwindled in contrast to its range of measurements but has vastly grown (mainly thanks to the development of precise electronic devices) as it now can read values from a

few mili-amperes to a few mega-amperes. Rogowski Coils have many features that explain why they are so popularly used in plenty of scientific experiments nowadays, instead of other current measuring devices, such as:

- They can endure large overloads without damaging;
- Measure currents in an extensive range;
- High flexibility combined with a light weight;
- Low cost;
- Electrically isolated from the main circuit.

Figure 2.5, taken from [24], illustrates the image of a Rogowski Coil and how it is correctly used in a RC integrator circuit.

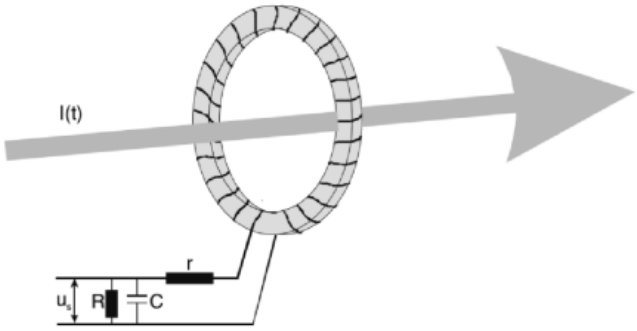

Figure 2.5: Rogowski coil with an RC integrator circuit.

It is through the relation between the current flowing across the Rogowski coil and the magnetic field variations along the axis (which induces voltage in the turns); that we can calculate the current values. By taking into account their cross-section and number of turns, we can express the proportionality of the induced voltage u(t), based on the value of current traveled i(t). It can be expressed by the equation, obtained by applying Ampere's law (Eq. 2.3) and then Faraday's law (Eq.2.4). In this equation, the symbol A represents the windings cross-section, s the number of turns per length unit, B the magnetic field produced by the current and N the number of windings.

$$i(t) = \frac{1}{\mu_0} \oint \vec{B}(t) \cdot d\vec{s} = \frac{s}{\mu_0} B(t) \tag{2.3}$$

$$u(t) = N\frac{d\phi}{dt} = N\frac{d(\int \vec{B}(t) \cdot d\vec{A})}{dt} = N\frac{A}{s}\mu_0\frac{di(t)}{dt} \tag{2.4}$$

Since the Rogowski Coil can be represented in the circuit as a component L, which value is equal to the sum of all self-inductance's of each winding; and integrator is needed

for deriving the current value (which can be configured by a simple RC circuit) it appears that we are now dealing with a RCL circuit, then we can rewrite the equation like so:

$$u(t) = \frac{d\phi}{dt} = Ri + L\frac{di}{dt} + \frac{1}{C}\int_0^t i dt. \tag{2.5}$$

Finally, it is important to establish that, thanks to its flexibility and the fact that the Rogowski coil always remains in a closed loop structure, the flowing current trajectory does not impact the output voltage. Considering there different types of Rogowski coils, as they can also be rigid (their internal material is magnetic) or have an active or passive integrator; it is important to know that high flexibility grants always an advantage to the device because it prevents magnetic saturation [25].

Since the magnetic field only changes with the correspondent current variation it should go without saying that the device is only capable of reading AC currents. Also, because its measurements are more accurate once there are no unexpected power losses in the integrator. We can also conclude that it would be beneficial that the windings of the coil are composed of superconducting materials in order for them to produce zero impedance. An example of this use can be found in [26].

3

Methodology and Project Setup

This chapter contains the planning research work along with some preliminary tasks and preparations essential for ensuring the successful execution of the upcoming experiments.

3.1 Method of Measuring AC Losses on the SFCL

In a quick recap, we have an iron cored transformer type SFCL, with superconducting windings in the secondary side of the transformer, that are being cooled by a cryostat with LN2. Independently if the loads are balanced or not, there are always power losses whenever a fault current appears, because of the inducted currents that operate in the normal conducting regions of these SC's. In order to measure these losses Rogowski coils will be added to those windings, so the values of the flowing current i(t), can be known. The SFCL alongside with one of the three cryostats is displayed in Figure 3.1, taken from [7].

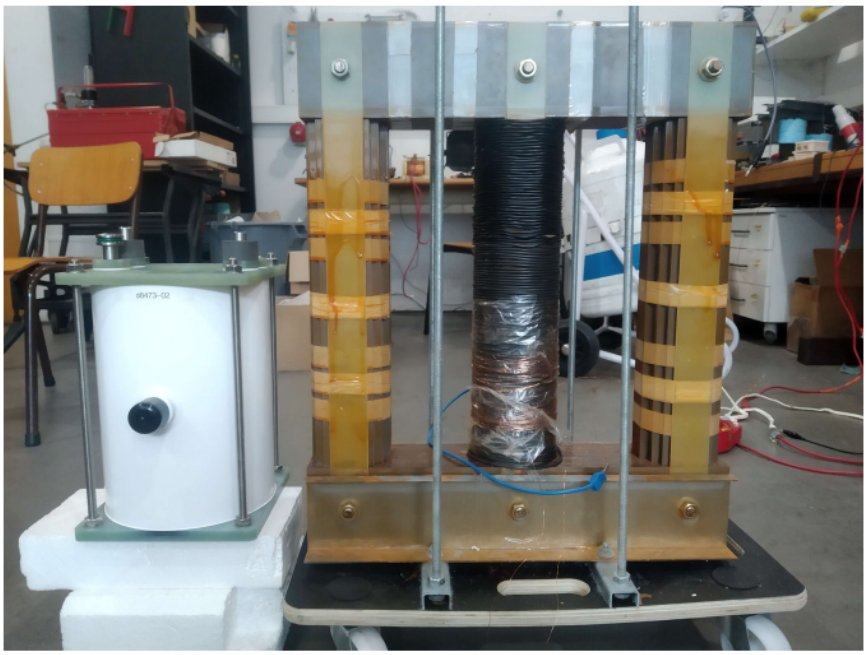

Figure 3.1: Image of the iron cored SFCL alongside with one cryostat.

These HTS windings, present in the secondary side of the transformer are made of a THEVA TPL5121 tape [27]. Through Figure 3.2, taken from [7], we can see that this specific tape is composed of many materials such as: a copper surround with an SnPb solder coating in the most external layers, the superconducting material GdBCO (that provides a strong magnetic shield [28], perfect for this experiment) above the Cap Layer, and between this layer and the substrate we have a buffer layer comprised of Magnesium oxide.

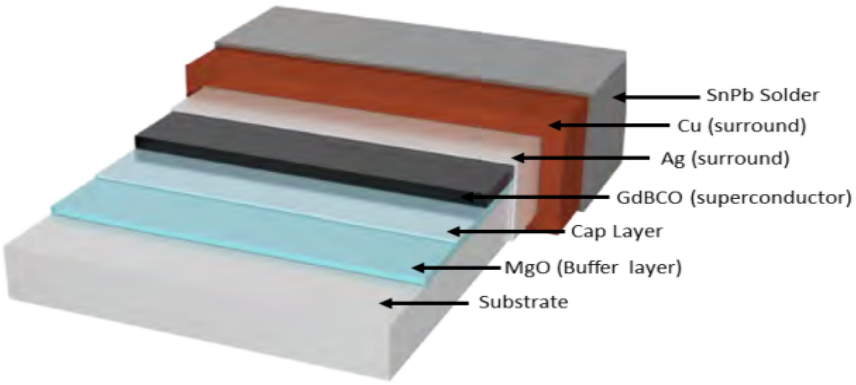

Figure 3.2: TPL5121 HTS tape layer configuration

The transformer that will be powered by a three-phased auto-transformer connected to an AC voltage with a range of 400 V.

The power losses can be calculated using the following expression:

$$p(t) = \epsilon(t) \times i(t) \tag{3.1}$$

where $\epsilon(t)$ corresponds to the instantaneous electromotive force present in the winding loop; and by simply integrating $P(t)$ for a chosen cycling period between T_a and T_b we get the average dissipated power:

$$P_{mean} = \frac{\int_{T_a}^{T_b} p(t)dt}{T_b - T_a} \tag{3.2}$$

This is made possible by the fact that the HTS windings are in a short-circuited closed loop.

The induced electromotive force, can be measured if it is known: the value difference of electric potential between two points u(t), the arc length between these two points l, and the perimeter of the loop d. As the following equation indicates:

$$\epsilon = \int_0^d \frac{u}{l} dx = u\frac{d}{l} \tag{3.3}$$

By directly connecting a voltmeter device to the superconducting windings, the values of U(t) can be obtained. However they are expect to be very low, so it may be necessary the use of calibrated amplifiers that will send an amplified signal to an oscilloscope so we can visualize the values. The following Figure 3.3, adapted from [7], showcases the many devices necessary for obtaining the values of $\epsilon(t)$ and i(t) and how the primary and secondary windings will be displayed around the iron core of the transformer.

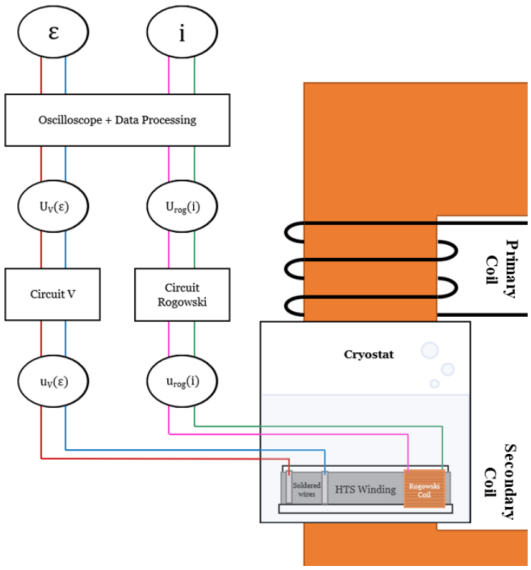

Figure 3.3: Data diagram of all the devices present in an operational HTS winding for this experiment (on one leg of the transformer).

In order to obtain the current values, i(t), a Rogowski Coil will be inserted to the HTS winding and then connected to integrator circuits, so it may reliably measure any

current that passes through its own toroidal hole. If the HTS winding provides virtually no impedance, then the coil will measure reliable results.

With k being the calibration constant, the current values can be calculated with the following equation:

$$i(t) = k \int u_{rog} \tag{3.4}$$

where u_{rog} is the voltage values obtained by the Rogowski Coil.

3.1.0.1 Assembly Method Used in the Experiments

This subsection details the assembly methods for measuring the AC losses of HTS Tapes and Windings, all the results of these measurements are present in the next chapter. All experiments start by using an auto-transformer as a variable AC voltage source, however there are some key differences to the system, depending whether we are trying to measure the AC losses of HTS Tapes or windings.

- **when measuring tape losses,** the auto-transformer was firstly connected to a single-phase transformer to provide a maximum of 4V to the system and a maximum of 100A worth of current. The transformer was then connected to the connected to the sample holder, with the sample already equipped with a Rogowski Coil that was then submerged in liquid nitrogen and put inside a styrofoam recipient.
- **when measuring winding losses,** the auto-transformer was instead connected to the primary and then to a resistive load of 1ω. Both the primaries and the cryostats were inserted into one leg of the SFCL iron core, with the primary being on top. The current in the primary would then induce another in the secondary winding contained inside the cryostat.

The two conductors attached to the samples (whether being HTS tapes or windings) were then connected to the Circuit V to amplify the voltage output of the sample and the Rogowski Coil was connected to the Circuit Rog to amplify and integrate the induced voltage output of the Coil. The resulting values were observed by an oscilloscope and then stored as Comma-separated Values files. They are saved in Pen drives and processed using a software code in Python that calculated the real values of the voltage and current of the sample as well as its energy losses and resistance values. This process is better explained in section 3.5.5.

3.2 Method of Measuring Solder Joint Resistances in DC

In order to measure the Solder Joint Resistances (R_{solder}) of the HTS Tapes, a current must flow through the joint, which also means it will pass through the superconducting layer. The superconducting layer exhibits AC resistance but no DC resistance below its critical

temperature, making DC current the most suitable choice for measuring joint resistance while the HTS winding tape is immersed in liquid nitrogen (LN2).

The measurements were carried out using a four-wire method, where a DC current source was connected to both ends of the created holder that held each tape, which were then laid in a Styrofoam based recipient and then fully submerged in LN2 to ensure they entered the superconducting state, eliminating DC resistance except for the solder joint resistance. The voltage drop between the conducting wires attached to the sample, was measured by a voltmeter for the various values of the injecting current. This method is illustrated by Figure 3.4.

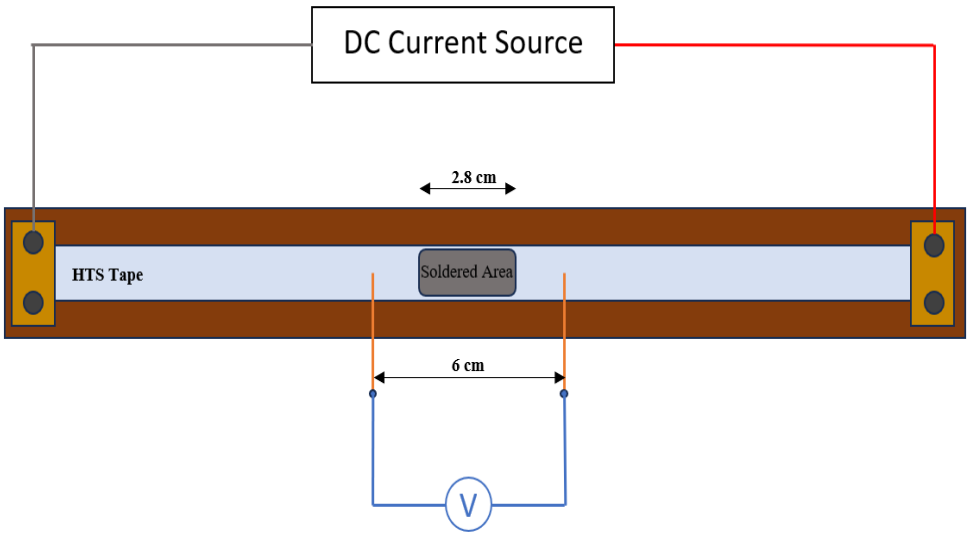

Figure 3.4: Diagram showcasing the method to measure the resistance of the HTS tapes

3.3 Method Proposed for Measuring the Electromotive Force

This section contains a proposition of a new method for measuring the electromotive force of HTS windings, that explains the measured results obtained in experiment 4.4 that differ from the expected values. Taking into account the experimental set up for measuring the AC losses of winding samples (as shown in Figure 3.5), we can represent an electric circuit in Figure 3.6, which translates it into the following equations, from 3.5 to 3.7. The symbols R_{sc1} and R_{sc2} represent the superconducting resistance external and internal to the voltage taps, respectively. While R_{lead} represents the resistance of the wires connected to the voltmeter, R_{joint} the resistance of the joint, and R_{volt} the internal resistance of the voltmeter. Finally, the currents i_{sc} and i_{volt} represent both the current in the superconducting winding and the current in the voltmeter.

Through the electric circuit, the following equation can be obtained:

$$\begin{bmatrix} R_{SC}+R_{joint} & -R_{joint}-2R_{SC2} \\ -R_{joint}-2R_{SC2} & R_{volt}+2R_{lead}+2R_{SC2}+R_{joint} \end{bmatrix} \begin{bmatrix} i_{SC} \\ i_{volt} \end{bmatrix} = \begin{bmatrix} -\frac{d\phi}{dt} \\ 0 \end{bmatrix} \tag{3.5}$$

Knowing that $R_{joint} >> 2R_{SC2}$, $R_{joint} >> 2R_{lead}$ and $R_{volt} >> R_{joint}$. We can reduce this equation to:

$$\begin{bmatrix} R_{SC}+R_{joint} & -R_{joint} \\ -R_{joint} & R_{volt} \end{bmatrix} \begin{bmatrix} i_{SC} \\ i_{volt} \end{bmatrix} = \begin{bmatrix} -\frac{d\phi}{dt} \\ 0 \end{bmatrix} \tag{3.6}$$

And from it, we can reach this final equation3.7. concluding that the measure voltage from the voltmeter is the product of the resistance of the joint with the flowing current in the superconducting winding.

$$V = R_{volt} i_{volt} = R_{volt} \frac{(R_{SC}+R_{joint}) i_{SC} + \frac{d\phi}{dt}}{R_{joint}} \tag{3.7}$$

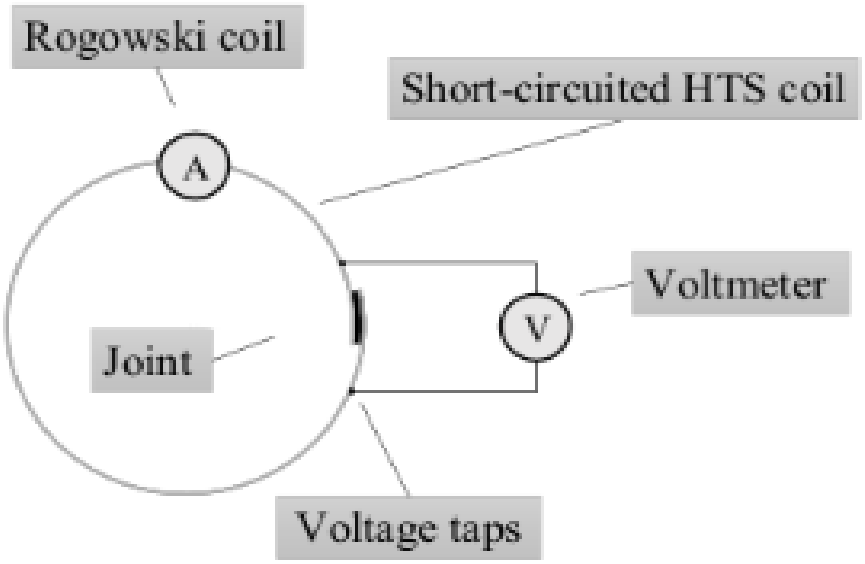

Figure 3.5: Experimental setup for the measuring AC losses of HTS winding samples.

3.4 Set up for the SFCL

Here are some tasks that were made to improve the Superconducting Fault-Current Limiter, in order to reduce the amount of defects that may occur and obtain the best possible loss measurements:

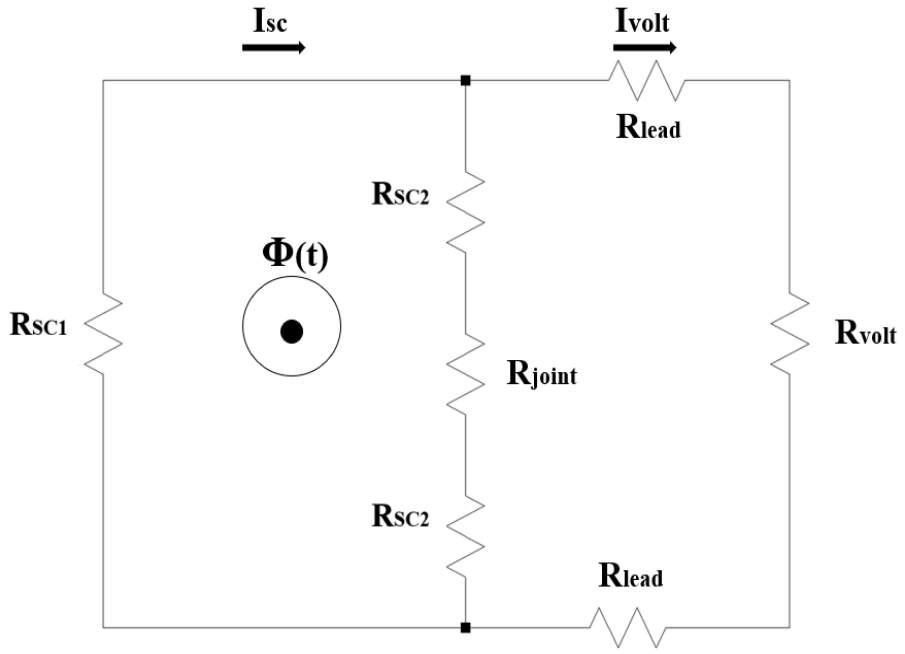

Figure 3.6: Diagram of the electric circuit equivalent to the setup.

3.4.1 Cryostats

The cryostat is the place where the HTS Winding samples are going to be placed and submerged with liquid nitrogen, with the cryostat already inserted into one of the legs of the transformer along with the primary windings on top. The transformer throughout the following experiments present in the upcoming chapters will always work as a single-phase transformer, with only one primary and secondary windings inserted into one of its legs.

Three identical cryostats were specially built and designed for this project, each containing several characteristics necessary for the execution of the experiments. They are the following:

- **Unique composition of the walls**, as the cryostat is constructed with G-10, also known as garolite, which is a fiberglass composite laminate. This material is ideal for cryogenic applications due to its high mechanical strength, low thermal conductivity, and coefficient of thermal expansion. Additionally, it provides excellent electrical insulation, which is crucial for preventing induction heating from the magnetic flux of the transformer. Moreover, as a non-inductive material, it does not interfere with the transformer's magnetic flux.

- **Vertical hole in the center of the cryostat and it's lid**, with a diameter around 0.5 cm larger than the diameter of the iron core, the cryostat can be easily inserted in each leg while also being close to the core.

- **Space for the LN2**, as it has a cylindrical shell cavity around the hole and inside the cryostat where the liquid nitrogen is stored.
- **Creates an insulation vacuum space**, as there is a small cavity surrounding the LN2 space, both inside and outside. It serves as a thermal conduction insulator using a vacuum, with its only connection to the exterior is via an isolation vacuum pump port (made of stainless steel) mounted on the exterior surface of the cryostat (displayed in Fig.3.7, taken from [7]). This port is where a turbo-molecular pump may be connected for periodic maintenance and then properly sealed afterwards.
- **Contains several fittings on the Lids**, these components serve specific functions: the electrical feed-through provides a hermetic connection to prevent gas leakage in and out of the cryostat; the LN2 fill port is where the liquid nitrogen is injected for storage; the vent port allows evaporated nitrogen to exit the cryostat through a check valve that releases the gas when pressure builds up; the vacuum pump port is used to decrease internal pressure in the cryostat but is sealed and unused in this experiment; and finally, there are four tie rods that clamp the lid to the base of the cryostat. These components can be observed in Fig 3.8, taken from [7].

(a) Top view (b) Front view

Figure 3.7: Top and front views of the cryostat.

Figure 3.8: Cryostat lid and all its respective fittings.

3.4.2 Designing the Primary Windings

For the primary windings, it was designed and 3D printed a model that can be perfectly placed above the cryostats, it also utilizes all the available space between those cryostats and the upper iron of the SFCL and, at the same time, is attached as close as possible to the iron core. The windings themselves were made of normal coppers wires, they were the chosen conductors thanks to their easy manufacturing and their relatively low price.

In total, three primary windings were made, each with a different amount of spirals, one with 10, another with 20 and the last with 40 spirals. The winding with 40 spirals is shown in Figure 3.9.

A more ideal method of designing primary windings would be to add in the future some appropriate modifications such as three terminals in each winding, positioned so they can measure current in 3 positions that are covered by a different number of spirals. But due to a lack of resources it was not possible to create such primaries.

Figure 3.9: Primary winding with 40 spirals.

3.4.3 Creating a New Mold to fixate the Secondary Windings

The HTS windings are to be placed in a cast, before being inserted inside the cryostat, so they remain sited in one place while operation, preventing measurement defects and possible damages to the samples and the connected wires. The old cast was made of a hard and inflexible material, which forced the HTS winding to have a gap greater than 20cm in length. Some samples were discarded because they did not fit into this cast. A new mold was then 3D printed with the exact same shape and appropriate measurements as the old one but it was made from a more flexible and less dense material, a thermoplastic polyester made with Polylactic Acid (PLA). The schematic of the mold is displayed on Fig I.1, present in the annex chapter I.

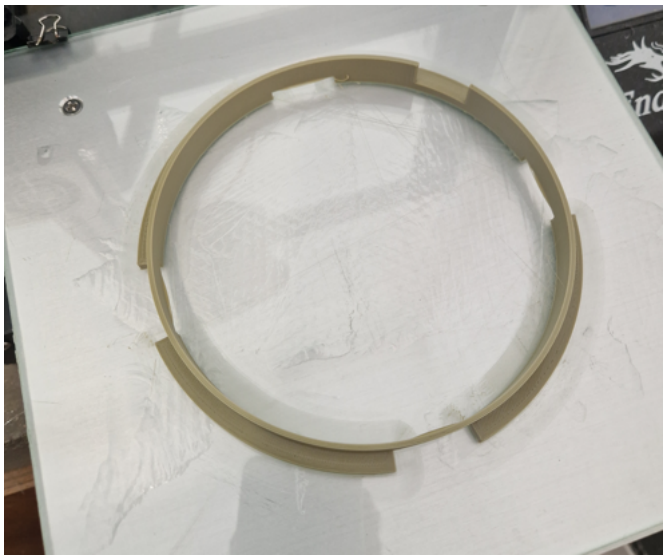

Figure 3.10: Cast for holding the HTS winding during operation.

3.5 Set up for the System Devices

Before conducting any experiments, it is crucial to confirm that all equipment in the system is properly calibrated and operational. Therefore, some integration adjustments to the system were carried out, followed by pre-experiment checks to ensure everything was set up according to the plan. There were also preformed tasks necessary that made sure other devices and equipments were in good working conditions and well integrated into the system in an adequate fashion, either removing and replacing damaged equipment or improving them. These tasks are described in the following subsections.

3.5.1 Production of HTS Tapes and Windings for the Secondary Windings

The use of a HTS winding is vital for the measurement of the AC losses, as the HTS tape, by itself, produce minimal AC losses. Therefore the measured AC loss values that are produced by the resistive soldered joint, fully represent the power losses of the system. However, in order to create a winding we need to solder the two extremities of a HTS tape, and that solder joint does add a significant resistance.

One objective of the upcoming experiments is the understanding of which materials are the best for soldering and what is the best method of jointing two segments of HTS tape that provide the lowest possible amount of resistance when a current is applied.

The secondary windings are single short-circuited turns made of THEVA TPL5121 tape, which is a second generation HTS tape. This tape has several layers made of different materials, as shown in Figure 3.2.

Initially, we made several viable samples, while most of were created using a lap joint, where a joint is made by lapping two ends together; three of them had a Bridge type joint, where a small segment of tape was used as a bridge on top of the two extremities, to solder them together as it is illustrated in Figure 3.11, adapted from [7]. Each sample was previously cleaned with chloridic acid before being soldered, the soldering area of every sample was 2.8cm and in the end added two copper wires to each end of the sample with a 6cm distance between them.

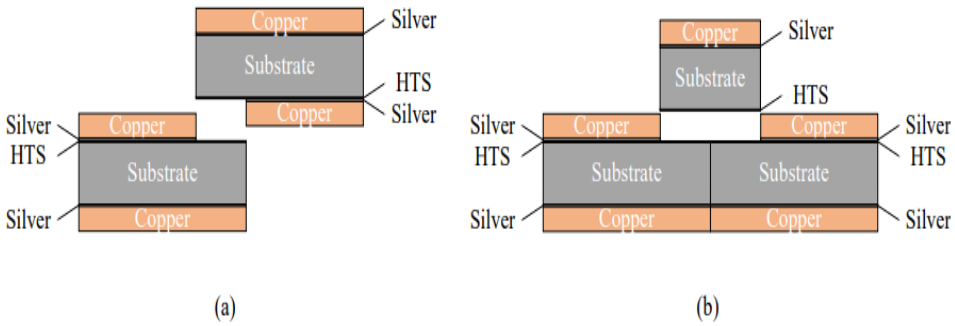

Figure 3.11: Types of joints. (a) lap joint. (b) bridge joint.

To assist the soldering, we used a small steel device to compress the solder points and at the same time to provide heat when the samples are put in the oven for a duration of 20 minutes and in a temperature 210 degrees Celsius. After the samples were sufficiently cooled we then soldered four wires to them; two current wires big and wide so they are capable of carrying large amounts of current, positioned in each extremity of the sample, and two thin voltage wires good for carrying low voltages, positioned between the current wires and the soldered zone. Finally a Kapton tape is applied around the HTS Windings and support to reduce the vibration amplitude due to the electromagnetic forces, the following Figure 3.12 shows the final result of one of the samples made.

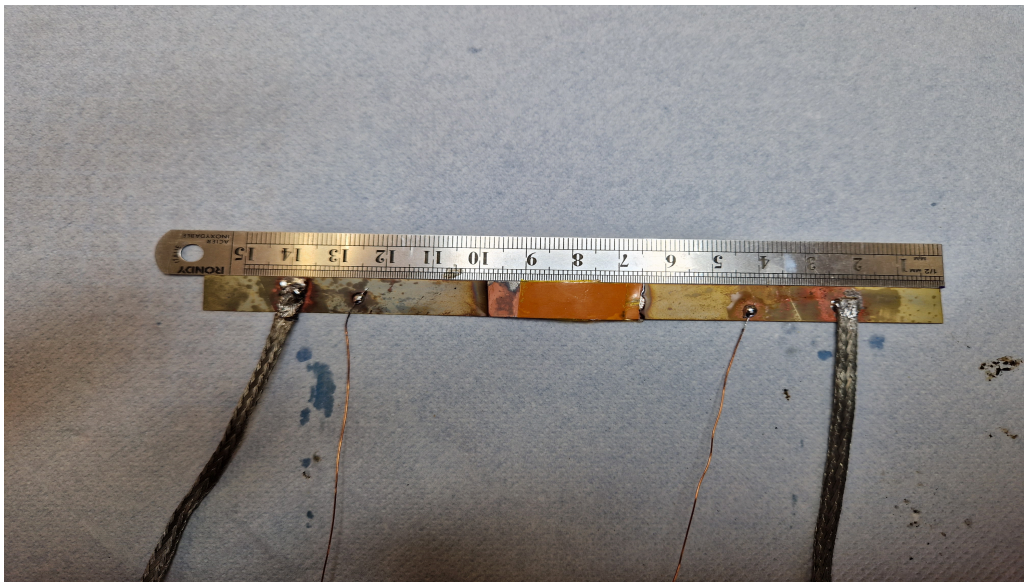

Figure 3.12: Image of one of the samples made.

While these initial samples were made with the assistance of Dr.Canan Aksoy, a PhD physicist at Karadeniz Technical University, and Diogo Durão. There was still the task to create three more bridge type tape samples myself using the sample method, however with different type of soldering pastes; all the while Diogo Durão and Dr. Canan created 3 more lap joint type windings for me to experiment. The experiments and results are shown in Chapter.4.

3.5.2 Cryostat instrumentation

Once each Rogowski coil was properly calibrated and then wrapped around the HTS (high-temperature superconductor) winding, the coils were secured in place with Kapton tape along with two 140 µm diameter phosphor-bronze wires were soldered to each Rogowski coil. Additionally, two more of these wires were soldered to each surface of the HTS winding, with a separation of 60 mm between them, for voltage measurement. These wire sets were twisted together to minimize induction picking. A photo of the instrumentation on the HTS winding is shown in Figure 3.13, taken from [7].

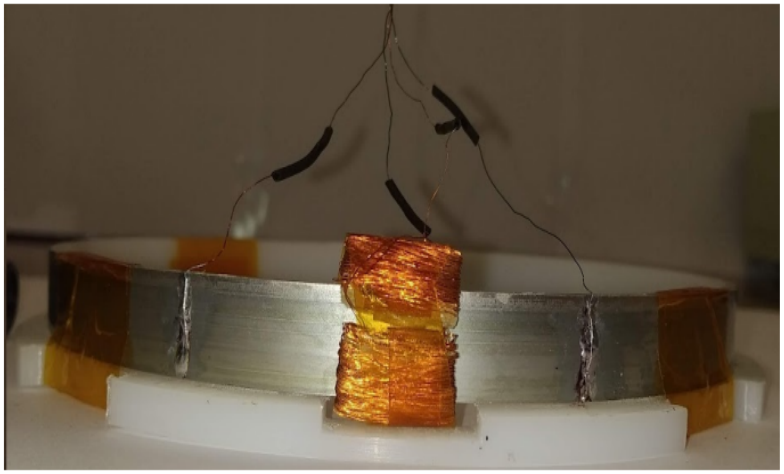

Figure 3.13: Photo of HTS winding on its support with rogowski coil and soldered wires for voltage measurement.

To reducing vibration during electromagnetic operation, tape was applied around the HTS winding. The wire sets were twisted together for increased mechanical strength and had a length of approximately 40 cm, with their ends soldered onto the male side of a raster signal plug. The female side of this plug had the ends of four 250 µm copper wires, which were also twisted together in sets of two and then twisted together again, with a length of around 20 cm. The other end of these copper wires was soldered to the hermetic connector of the cryostat lid, establishing an external connection for the Rogowski coil and the 6.0 cm voltage measuring points of the HTS winding. A visual representation of this experimental assembly can be seen in Fig 3.14, taken from [7].

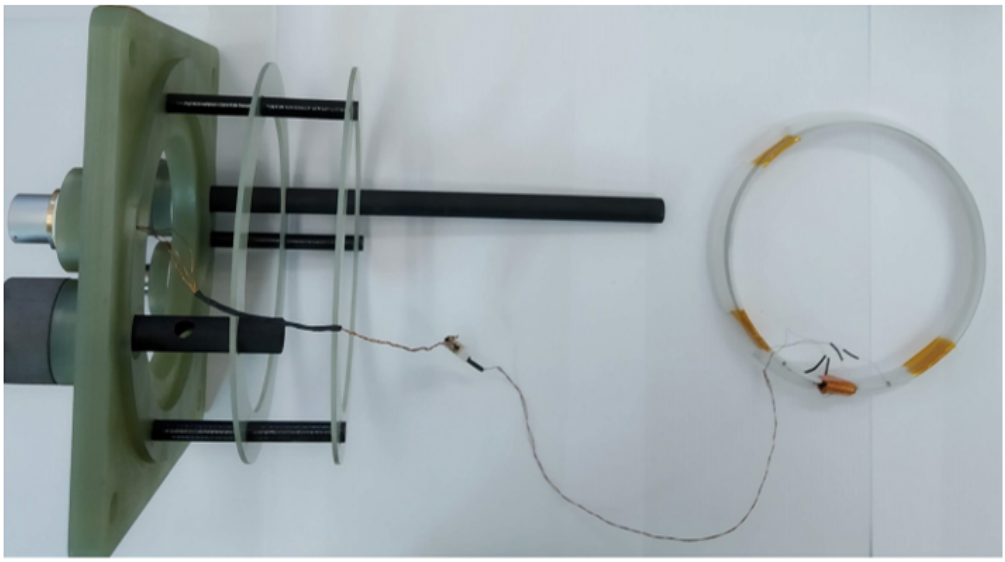

Figure 3.14: Photos of cryostat lid with HTS winding connected.

After fully equipping the three cryostat lids, each must be properly closed. This prepares the cryostats for the experiments, once they are inserted into their respective leg

in the iron core. The HTS windings can enter the superconducting state by filling their respective cryostats with LN2. This is done by pouring the liquid nitrogen into the LN2 fill port with the vent port open. After filling the cryostat with enough LN2, both ports are closed using their respective check valves. With the instrumentation of the three cryostats ready, the next step is to conduct experiments and obtain the results of the three HTS windings in a single-phase setting.

3.5.3 Creating a new holder for the HTS Tapes

This new holder was created for the necessity of holding the HTS tapes in place and prevent their movement during measurements for their joint resistance, the holder was made out of tufnol kite which is an non magnetic material with with good mechanical behavior at liquid nitrogen temperature; the holder can be seen in Figure 3.15. On top two copper plates, on each side of the basis, where held by two screws attached to the tufnol kite. The HTS tape samples are then to be placed between the plates, then the screws are tightened in order for the samples to remain fixed throughout the experiments. In order to provide current to the samples two 0.5cm wide copper wires are attached to the basis, connecting it to the current source. Lastly, the basis with the sample is placed inside a styrofoam box where is latter submerged with liquid nitrogen.

Figure 3.15: Holder for the HTS tapes during operation.

3.5.4 Electronic Circuits

As seen in Fig.3.3, each HTS winding needs to be connected to a specialized circuit (Circuit V) that amplifies the signal, acting as an Instrumentation Amplifier; and also a Circuit Rogowski that not only Amplifies the voltage obtained by the coil,U_{rog}, but also Integrates

the signal. This means that, in total, there are three Circuit V's and three Rogowski Circuits, nicknamed respectively for each system V1 and Rog1, V2 and Rog2, V3 and Rog3.

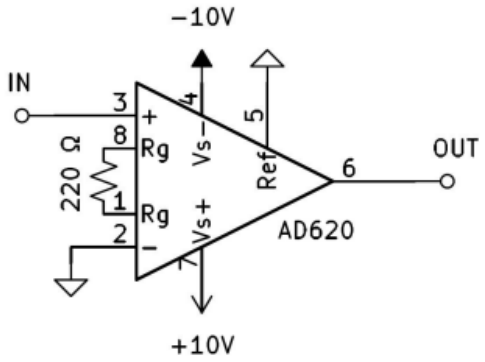

Figure 3.16: Example of a schematic of circuit V.

Circuits V1, V2 and V3 are simple AD620 amplification circuits, with their schematic displayed in Fig.3.16, taken from [7]. After building these three circuits, each one of them will be calibrated by measuring with an oscilloscope their respective amplitude values of the input sinusoidal signal, originated from a wave generator, and their output amplitudes.

The Rogowski coils will be connected to their respective circuit and calibrated together by wrapping it around a HTS tape. That aforementioned tape is then put in series with a circuit that has a known AC current by measuring the voltage between the terminals of an 1Ω resistance. This resulting electrical circuit will help in the calibration of Rogowski coil system present in Figure 3.17), taken from [29].

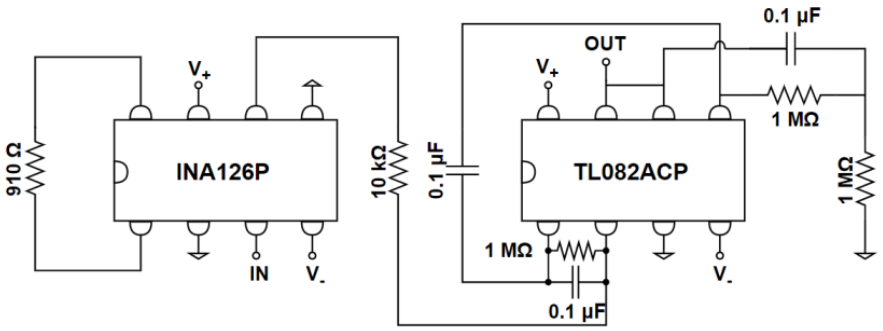

Figure 3.17: Assembly used for calibrating the rogowski coils.

By measuring with the help of an oscilloscope, the different AC currents with the respective voltage outputs from Circuit Rog, it is possible to fit using linear regression the output of Rogowski coil, together with the Circuit Rog, with the current of the calibration circuit.

3.5.4.1 Creating new Rogowski Coils for the HTS Windings

Two of the previously used Rogowski Coils were damaged and could no longer be operable, this happened due to the fragility of the copper wires used. Therefore two new ones were made, this time using wires with a higher diameter, it granted the coils more rigidity but at the same higher resistance then the old ones. One of the new coils can be seen in Figure 3.18. Both of them were tested and calibrated by using attaching them to a HTS Tape with no Joint while injecting AC current, the corresponding voltage was then amplified and integrated by a Rogowski Circuit and the output signals were then measured for different values of the input current; lastly it was possible to fit using linear regression the output of each Rogowski coil along with its corresponding circuit. These are the resulting equations:

- **Circuit Rog1 (No Colour)**: $I = (41.1)U_{out} - 0.002; R^2 = 0.9998$
- **Circuit Rog2 (Orange)**: $I = (530.5)U_{out} - 25.935; R^2 = 0.9981$
- **Circuit Rog3 (Green)**: $I = (198.7)U_{out} - 7.586; R^2 = 0.9972$

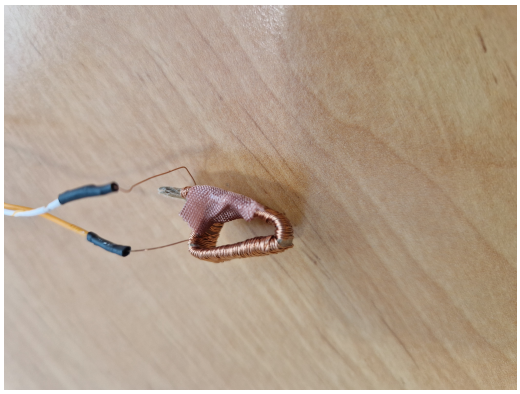

Figure 3.18: Orange rogowski coil with a small adhesive tape to keep it's shape.

3.5.4.2 Analyzing and Improving the Measuring Devices

In order to prevent any accidents or mistakes that may interfere with the whole system every measuring device was tested before any experiment was made. The Oscilloscopes, the three Circuit V's and the Rogowski circuits as well, were tested and their measured values indicated that they were well implemented and functioning properly.

In regards towards the amplification properties of the Circuit V, it was tasked to increase their gain. The resistance was changed for circuits V1 and V3, when tested the calibration equations and coefficients, determined by the linear regression curve, were as such:

- **Circuit V1**: $U_{in} = (2.2) \times 10^{-3} Uout - (4) \times 10^{-4}; R^2 = 0.9984$

- **Circuit V2**: $U_{in} = (4.1) \times 10^{-3} Uout - (2) \times 10^{-5}; R^2 = 0.9999$
- **Circuit V3**: $U_{in} = (9.3) \times 10^{-4} Uout - 5.3003; R^2 = 0.9915$

3.5.5 Data Processing

In this project, it is necessary the creation of a software program capable of gathering and processing the data measured by the superconducting coils, and from the cryostat as well, so we can reach some conclusions about what forces are currently at play during the procedures and how do the many components of the project behave in relation to each other.

The chosen program for this project was a Python program created in Jupyter Notebook to process all the CSV data collected during the single-phase and three-phase experiments. The program was originally authored by Diogo Durão, but later some changes were added.

The first step of the program involves storing the data from each CSV in three arrays, each holding specific information: Time, Channel 1 (containing the u_v data), and Channel 2 (containing the u_{rog}). Two different oscilloscope models were used in this experiment, each storing their CSV data in various formats. As a result, a function was created for each model to transform their data into a unified array structure.

Once the arrays are constructed, the voltage values within them are converted into meaningful ϵ and i data. This calculation is performed as follows:

- **For obtaining the values of ϵ**: The u_v data acquired from the Channel 1 is going to be multiplied by $\frac{L}{l}$, to obtain ϵ according to the Circuit V calibration equations of 3.5.4, as U_v now becomes u_v. Following eq.3.3, with l corresponding to the 60 mm separation between the voltage points and L representing the perimeter of the winding, corresponding to a total length of 438.3 mm, since each winding has a diameter of 139.5 mm. Thus, ϵ is obtained by multiplying u_v by 7.3.
- **For obtaining the values of i**: The u_{rog} data acquired from the Channel 2, will directly translate into i by applying the Circuit Rogowski calibration equations of 3.5.4.

After the ϵ and i arrays are built, the datasets are properly prepared before calculating the power losses. The program starts by smoothing the data with a moving average filter using hanning windows with chosen sizes (a larger window filters more). The SciPy library is then used to identify and store the positions of the relative peaks and valleys of the smoothed ϵ and i signals. Since the output of the circuits contained unintended DC voltage, the program removes this component by calculating the average of the smoothed signal between its first peak and last peak, then subtracting it from the pre-smoothed and smoothed ϵ and i data. The resulting plots are created to show the pre-smoothed and smoothed signals (with their average now removed) as well as their respective peaks and valleys, allowing the user to visually inspect the smoothing, peak finding, and

average removal process. Additionally, the program generates a time-series plot with both smoothed ϵ and i for each attempt saved during the experiment, enabling the user to visually observe and study the phase difference between ϵ and i.

To calculate the power losses, the program creates an array for each filled saved attempt with the product of ϵ and i (as stated in equation 3.1), which calculates the instantaneous power of the HTS winding during the attempt. The program also generates a time-series plot so that users can study the power behavior over time. Peaks and valleys of these signals are detected and recorded. Finally, the average power loss of an HTS winding during a cycle, P_{mean}, is calculated by the program using equation 3.2, where T_a is the time instant of a peak and T_b is the time instant of another peak, with $T_b > T_a$. This integral is calculated using the "integrate.trapezoid" function of numpy, with T_a and T_b generally referred to as the first peak and last peak respectively. By obtaining the average amplitudes of each current signal, the program creates a plot for the system with the current amplitudes, I_{AMP}, as the horizontal values and the average power loss, P_{mean}, as the vertical values. With this program, all the data was successfully processed.

4

Experiments and Discussions

This section contains the results of both the energy losses and Solder Joint Resistances measured during the experiments, along with an analysis. The energy averages, denoted by Q, are measured in mJ per cycle. In this context, a cycle refers to the power grid cycle, which has a frequency of 50 Hz, equivalent to a duration of 0.02 seconds. The experimental data was fitted to power law functions of the form $Q = \alpha I_{Amp}^{\beta}$, where α is a real coefficient and β is a real exponent. The decision to use these functions was made after examining the graphs and noting that most of the fits had good quality, as measured by the Normalized root mean squared error (NRMSE). The NRMSE is calculated as the root mean squared error divided by the energy range, which is the difference between the maximum and minimum energy values. In this study, a fit is deemed valid if it has an NRMSE of less than 0.05.

The fitting process is done indirectly by linearly fitting $ln(Q) = ln(\alpha I_{Amp}^{\beta}) = ln(\alpha) + \beta ln(I_{AMP})$ to obtain the values of α and β. It is important to note that in this type of fitting makes the fits more accurate for higher energy values but less accurate for lower ones. To better study the nature of the superconducting secondary, phase shifts between ϵ and i were calculated by finding the maximum argument of the cross-correlation between the two signals.

4.1 HTS Tapes Solder Joint Resistances in DC

This section contains the experiments made for measuring the R_{solder} of multiple HTS Tapes, using the method described in section 3.2. With these experiments the aim of understanding which solder type materials provide less resistance for HTS Tapes.

The assembly of all devices used for this experiment is shown in the figure 4.1.

4.1.1 Results and Discussion

In total 3 HTS tapes were made: Samples E, G and H; each were made with a different soldering paste, but all had bridge-type joints. While sample E was made with Sn60Pb40 soldering paste, G was made with Sn99Cu1 and H was made with a special

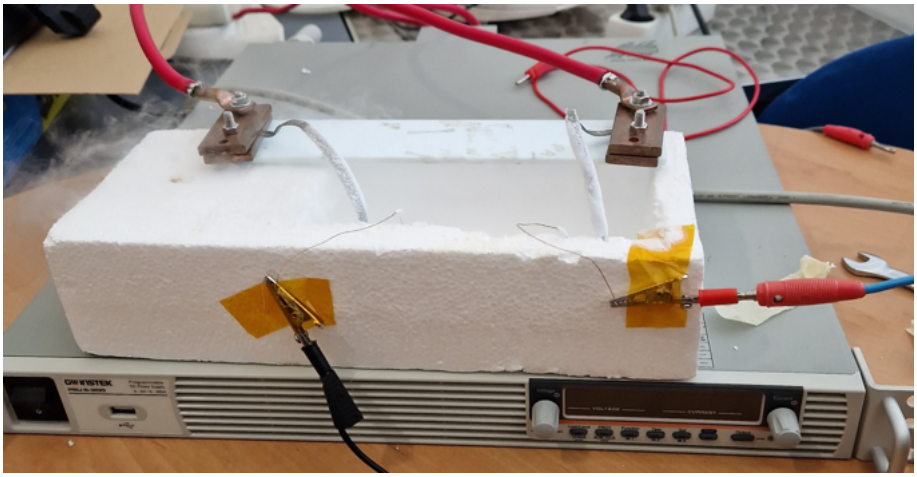

Figure 4.1: Assembly for measuring the resistance of the created samples.

paste (CHIPQUIK SMD291SNL15T4). There is no unique characteristic that differentiates each tape beyond the the type of solder paste, as they were all created using the same method described in section 3.5.1

By linearly fitting the voltage and current data and applying Ohm's law, the solder resistance for each HTS tape segment was calculated. The results are displayed in the following figure 4.2.

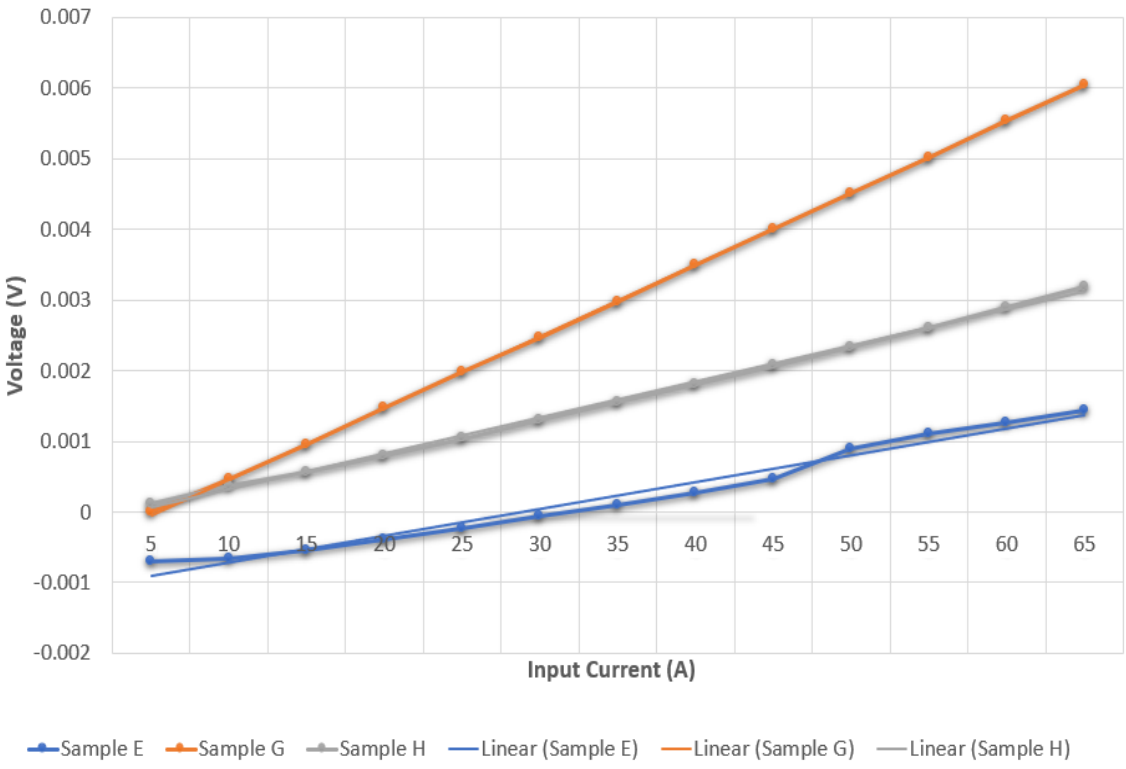

Figure 4.2: V-I curve of HTS tape joints.

Here are the respective resistance of each sample:

- **Sample E**: $R = (3.80) \times 10^{-5}\Omega; R^2 = 0.9767$
- **Sample G**: $R = (1.01) \times 10^{-4}\Omega; R^2 = 0.9999$
- **Sample H**: $R = (5.01) \times 10^{-5}\Omega; R^2 = 0.9984$

In the end we concluded that the best solder type materials were the ones used in sample E, that reached the lowest R_{solder} value of $3.8 \times 10^{-5}\Omega$. So we can conclude that creating HTS Solder joints with the solder paste used in sample E grants a lower resistances for HTS windings than using any of the two other solder pastes.

4.1.2 No joint Experiment

For this experiment, a simple HTS tape segment was used with the intention of observing the sample in its superconducting state. When that phenomenon occurs, the tape itself does not provide any resistance and thus the relation between the inserted Current and the output Voltage is no longer described by a linear curve ($U = RI$), because the Voltage would be null, instead what the multimeter would show is the resulting power created by the sample, whose values would be translated by a power curve ($P = \alpha(I_{amp})^2$).

However the results measured in this experiment were unexpected, as they do not resemble a power curve as it is shown on the image below.

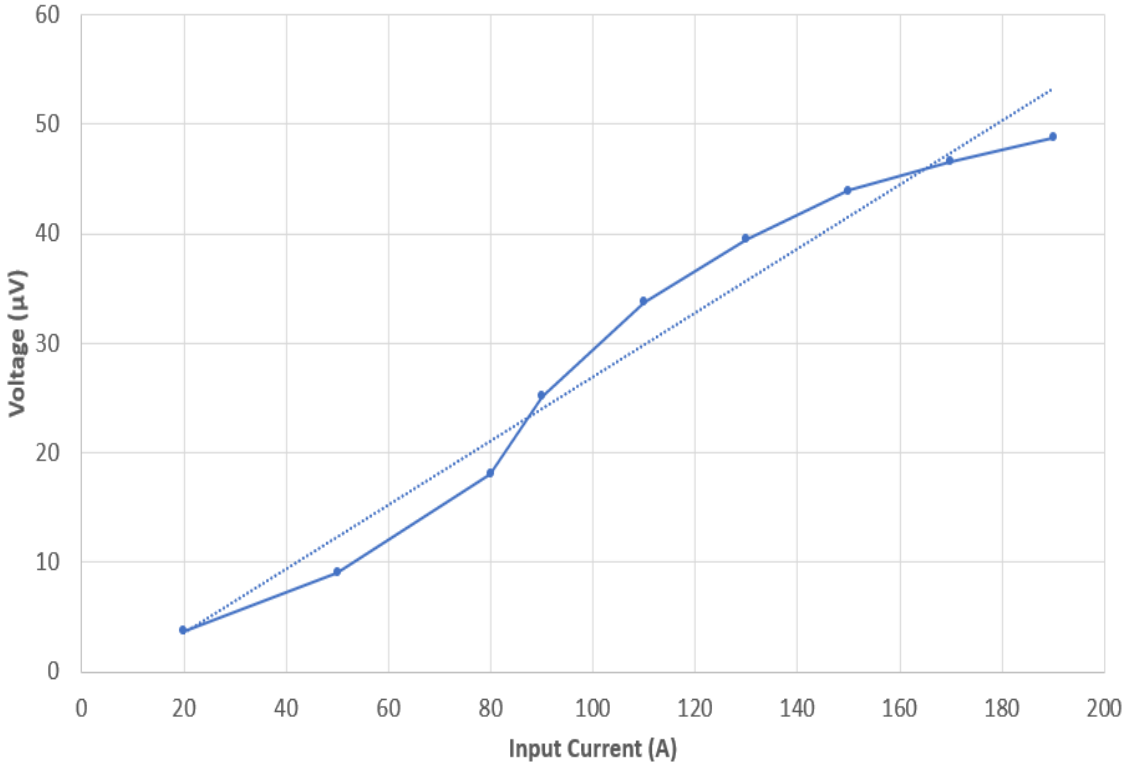

Figure 4.3: Measured values of the no-joint sample.

Instead it more resembles a linear curve, a possible reason for this behavior might be that either the amplifiers are not correctly amplifying the small signal increments, or perhaps the tape holder is likely providing a resistance to the sample, although with considerably low values of $2.927 \times 10^{-7}\Omega$.

4.2 Tape AC Losses

This section contains the measured losses of the samples E, G, and H, using the method described on 3.1. It is worth remind that the only distinguishable difference between each sample is their solder type materials.

4.2.1 Sample E

In this subsection are displayed the registered values while measuring the AC losses of the E sample, including its highest and lowest values of registered current and voltage, the calculated power losses and the average Impedance values of the tape.

In total, nine SQL files were taken during the experiment. The following figures show the registered values of the current, $I(A)$, and voltage, $U(V)$, for the highest and fourth lowest values of current I_{AMP}. These results were registered within a time frame of $[-0.2; 0.2]$ seconds.

The average calculated phases between electromotive force, ϵ, and the induced current, i, throughout all data files, are close to 0° which shows the highly resistive nature of the winding sample E. The graphs of the lowest and highest current amplitudes can be seen in figure 4.4, where ϵ and i can be read respectively in the left and right vertical axis.

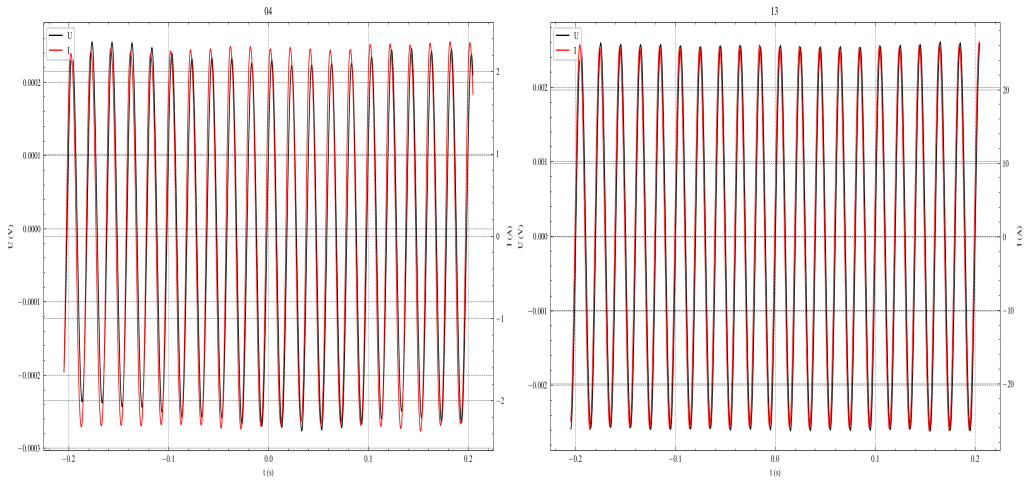

Figure 4.4: Time graphs of electromotive force and current of sample E for the highest and lowest values of I_{AMP}

The average energy for each measurement can be seen in Fig 4.5, with it's respective fit curve which is described by the equation $Q_{fit} = (1.07 \times 10^{-3})I^{1.96}$ with a fit quality of

NRMSE= 0.013. This equation is really similar to the power calculated by using Ohm's Law, RI^2, which proves that the sample's behavior is practically ohmic.

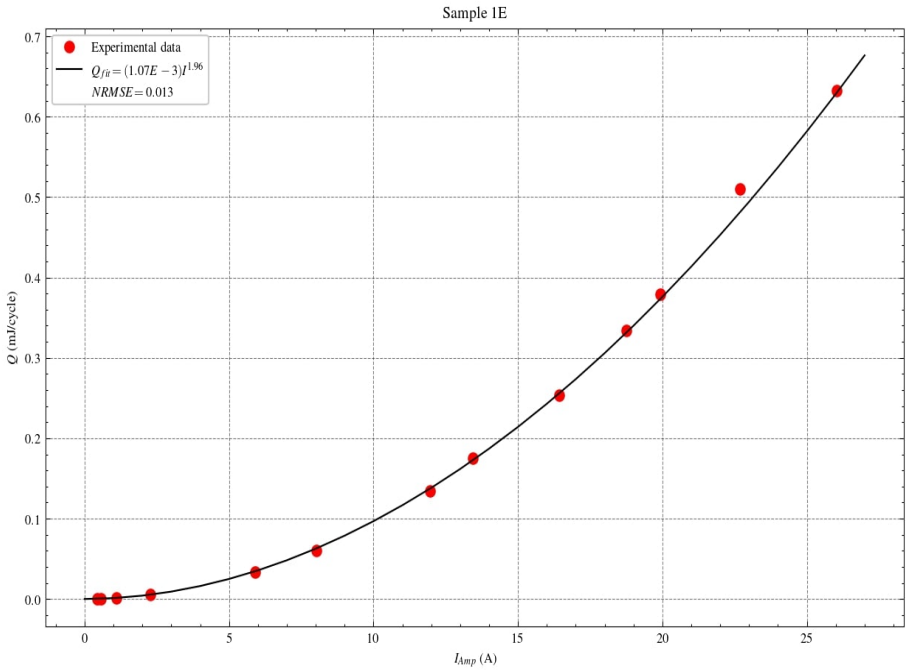

Figure 4.5: Graph of calculated average energies for single-phase sample E and respective power law fit curve in relation to current amplitude

Finally, the average resistance of the sample was calculated in Fig 4.6, with its respective fit curve which is described by the equation $U = (9.94 \times 10^{-5})I - (1.28 \times 10^{-5})$; $R^2 = 0.996$

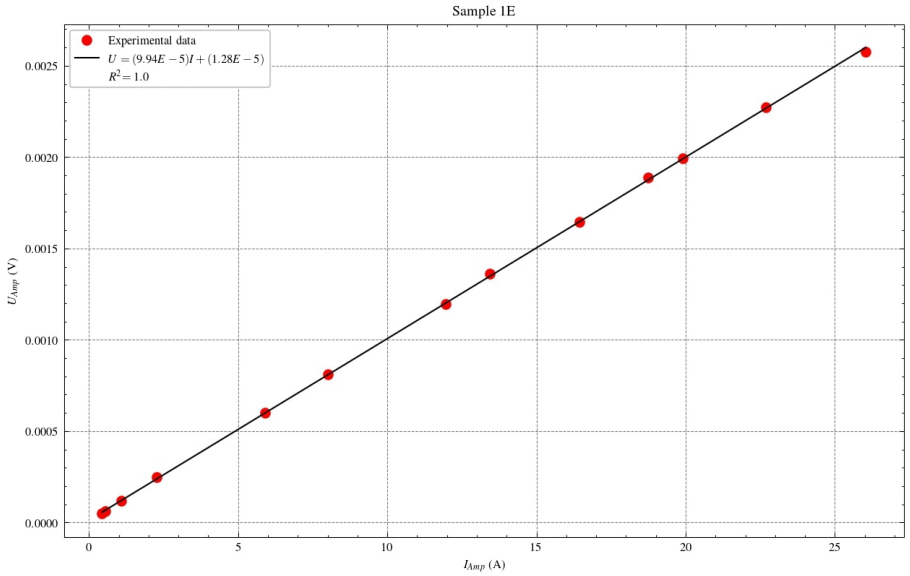

Figure 4.6: Graph of calculated average Resistance for single-phase sample E and respective linear fit curve in relation to current amplitude

4.2.2 Sample G

In this subsection are displayed the registered values while measuring the AC losses of the G sample, including its highest and lowest values of registered current and voltage, the calculated power losses and the average Impedance values of the tape.

In total, five SQL files were taken during the experiment. The following figures show the registered values of the current, $I(A)$, and voltage, $U(V)$, for the highest and lowest values of current I_{AMP}. These results were registered within a time frame of $[-0.10; 0.10]$ seconds.

The average calculated phases between electromotive force, ϵ, and the induced current, i, throughout all data files, are close to 0° which shows the highly resistive nature of the winding sample G. The graphs of the lowest and highest current amplitudes can be seen in Fig. 4.7, where ϵ and i read respectively in the left and right vertical axis.

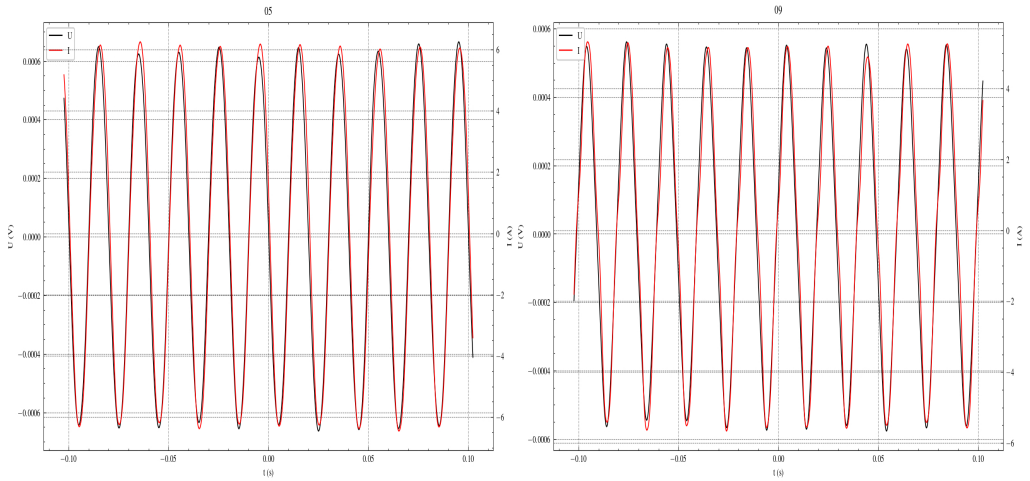

Figure 4.7: Time graphs of electromotive force and current of sample G for the highest and lowest values of I_{AMP}

The average energy for each measurement can be seen in Fig. 4.8, with its respective fit curve which is described by the equation $Q_{fit} = (1.04 \times 10^{-3})I^{1.98}$ with a fit quality of NRMSE= 0.081. This equation is really similar to the power calculated by using Ohm's Law, RI^2, which proves that the sample's behavior is practically ohmic.

Finally, the average resistance of the sample was calculated in Fig. 4.6, with its respective fit curve which is described by the equation $U = (1.00 \times 10^{-4})I + (1.92 \times 10^{-5}); R^2 = 1.0$

The Resistance calculated from this experiment is very similar to the results obtained in the DC experiments, so we can confirm that the experiment turned out as expected.

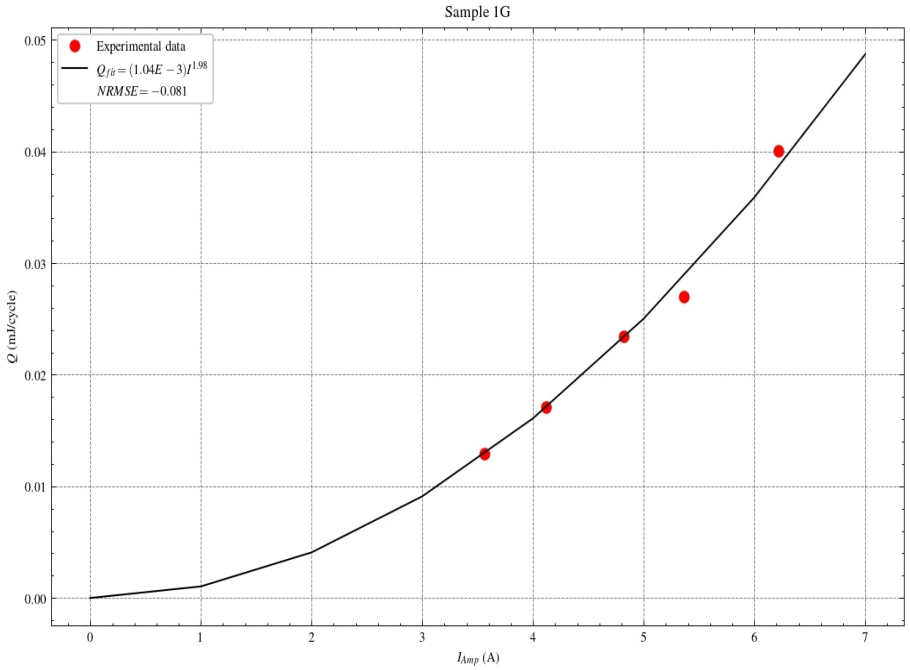

Figure 4.8: Graph of calculated average energies of sample G and respective power law fit curve in relation to current amplitude

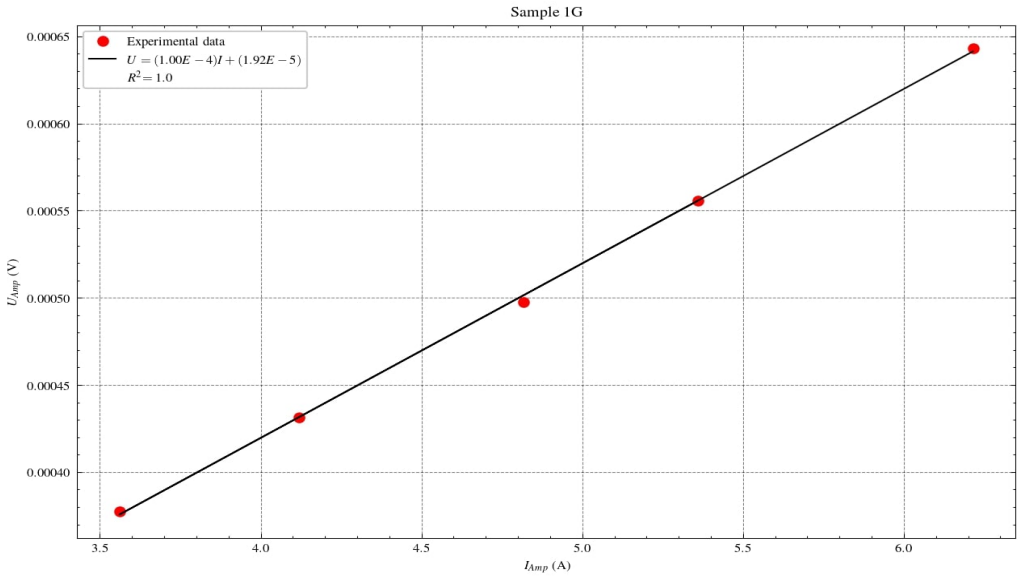

Figure 4.9: Graph of calculated average resistance values of sample G and respective linear fit curve in relation to current amplitude

4.2.3 Sample H

In this subsection are displayed the registered values while measuring the AC losses of the E sample, including its highest and lowest values of registered current and voltage, the calculated power losses and the average Impedance values of the tape.

In total, ten SQL files were taken during the experiment. The following figures show the registered values of the current, $I(A)$, and voltage, $U(V)$, for the highest and lowest values of current I_{AMP}. These results were registered within a time frame of $[-0.02; 0.02]$ seconds.

The average calculated phases between electromotive force, ϵ, and the induced current, i, throughout all data files, are close to 0° which shows the highly resistive nature of the winding sample H. The graphs of the lowest and highest current amplitudes can be seen in Fig. 4.10, where ϵ and i read respectively in the left and right vertical axis.

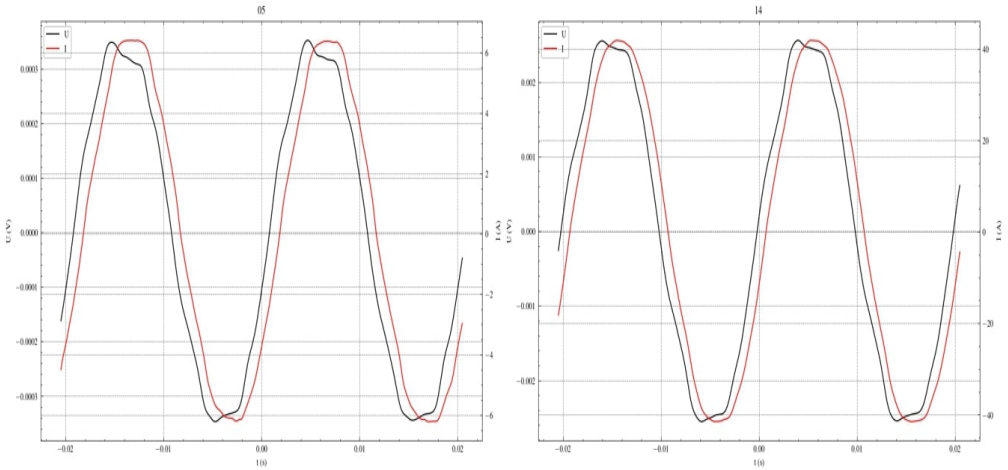

Figure 4.10: Time graphs of electromotive force and current of sample H for the highest and lowest values of I_{AMP}.

The average energy for each measurement can be seen in Fig.4.11, with its respective fit curve which is described by the equation $Q_{fit} = (5.13 \times 10^{-4})I^{2.05}$ with a fit quality of NRMSE= 0.016. This equation is really similar to the power calculated by using Ohm's Law, RI^2, which proves that the sample's behavior is practically ohmic.

Finally, the average resistance of the sample was calculated in Fig.4.12, with it's respective fit curve which is described by the equation; $U = (6.31 \times 10^{-5})I - (9.43 \times 10^{-5})$; $R^2 = 0.996$.

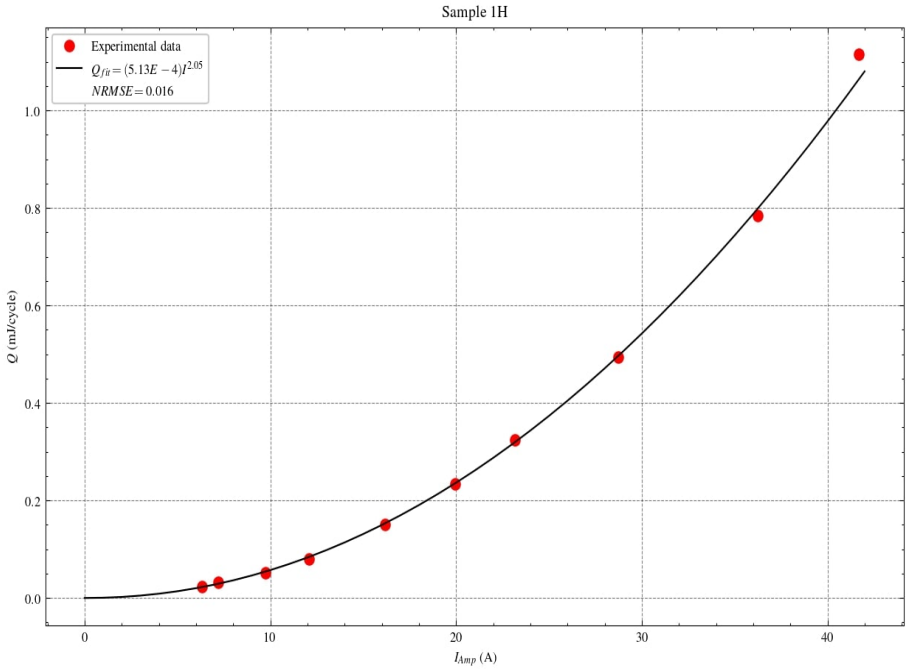

Figure 4.11: Graph of calculated average energies for single-phase sample H and respective power law fit curve in relation to current amplitude

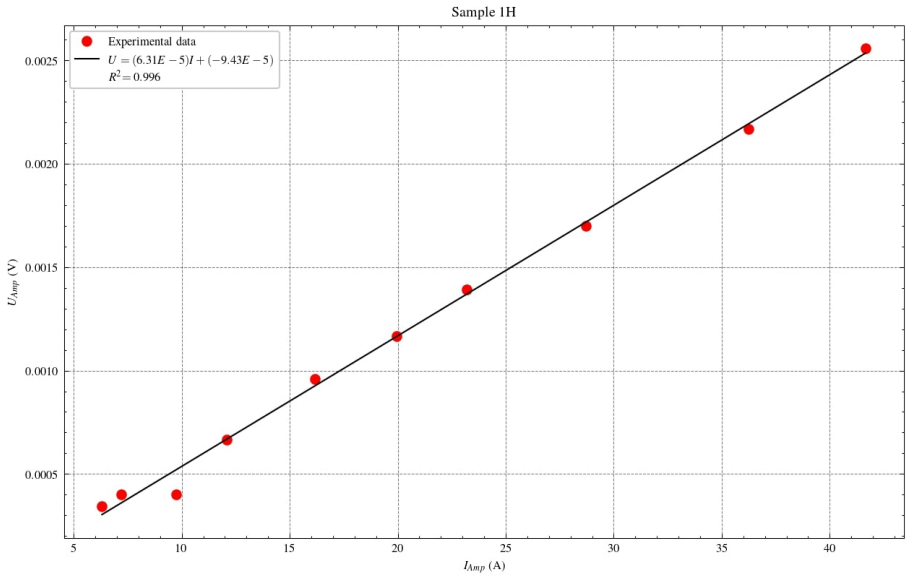

Figure 4.12: Graph of calculated average Resistance for single-phase sample H and respective linear fit curve in relation to current amplitude

Sample Name	α	β	Resistance (Ω)
Sample E	1.07×10^{-3}	1.96	9.94×10^{-5}
Sample G	1.04×10^{-3}	1.98	1.00×10^{-4}
Sample H	5.13×10^{-4}	2.05	6.31×10^{-5}

Table 4.1: AC power losses and resistance values of each sample.

4.2.4 Discussion

Based on the calculated results present in Table 4.1 we are able to observe that, as expected, the R_{solder} values of samples E and H are higher when injecting AC current then when injecting DC current. This is thanks to the fact that some AC losses are generated due to the movement of magnetic vortices within the superconductor when experiencing time-varying currents or magnetic fields (or both). There was a noticeable high increase of 1.61 times higher R_{solder} for sample E, and a slight increase of 26% for sample H; but the R_{solder} values for sample G remained the same. This concludes that some solder type materials have a bigger negative reaction to the AC currents than others, that raises the power losses of the samples and raises the original R_{solder} values of the sample. Therefore the solder used in sample H (CHIPQUIK SMD291SNL15T4) contains materials that cause lower energy losses then the other samples, as the α of the sample reached the lowest value of 5.13×10^{-4}.

4.3 AC Winding Losses Using the SFCL (with iron core)

In the single-phase experiments, each HTS winding was separately experimented, and thus, this section will be subdivided to show the acquired results for each winding.

4.3.1 Samples with bridge-type joints

The measuring method for these experiments is the same one described on 3.1, and the samples used were two new HTS Windings with bridge-type joints dubbed samples I and J. However at the time they could not be attached to the old mold, and thus it wasn't safe for them to be placed inside the cryostat. So instead they were put in a styrofoam box with a hole in the middle so it could be connected to the iron-core of the SFCL. This time the only difference between each tape is that sample J has twice the solder junction area of sample I (5.6cm). The assembly of all devices used for this experiment is shown in the figure 4.13.

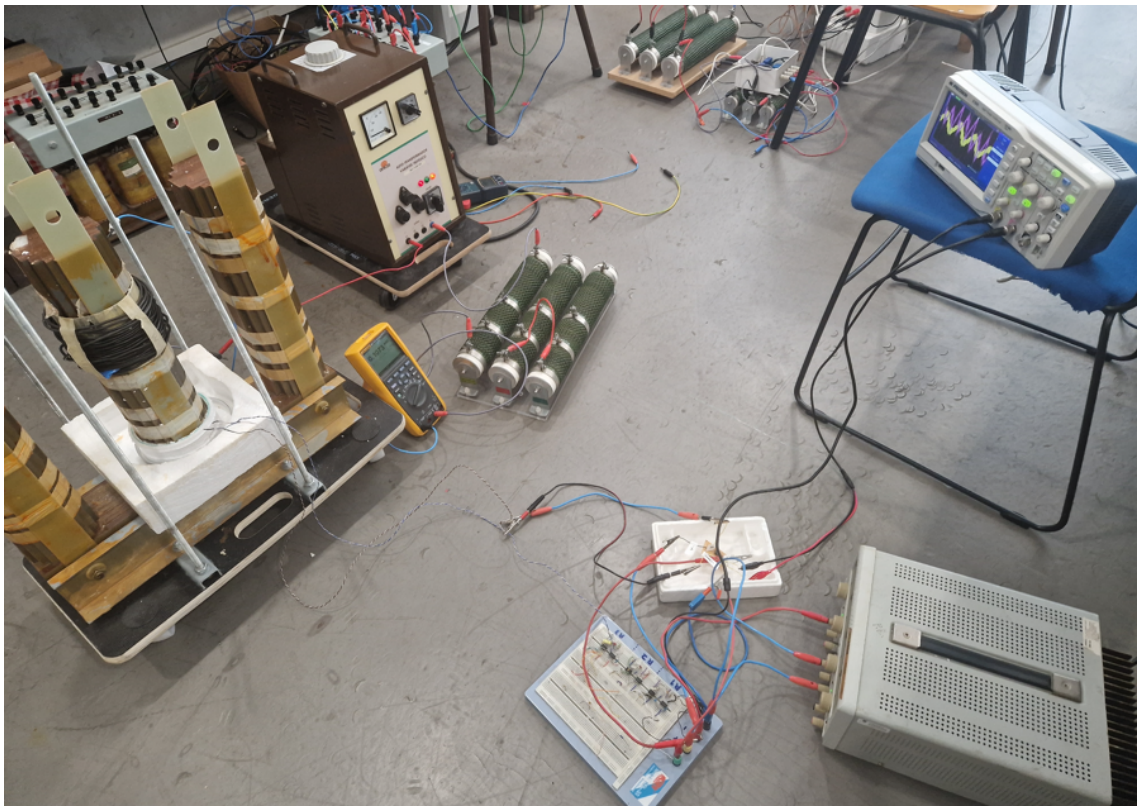

Figure 4.13: Assembly of all equipments for the measuring the ac losses of the bridge-type windings.

4.3.1.1 Sample I

In this subsection are displayed the registered values while measuring the AC losses of the I sample, including its highest and lowest values of registered current and voltage, the

calculated power losses and the average Impedance values of the tape.

In total, twelve SQL files were taken during the experiment. The following figures show the registered values of the current, $I(A)$, and voltage, $U(V)$, for the highest and lowest values of current I_{AMP}. These results were registered within a time frame of $[-0.04; 0.04]$ seconds.

The average calculated phases between electromotive force, ϵ, and the induced current, i, throughout all data files, are close to 0° which shows the highly resistive nature of the winding sample I. The graph of the highest current amplitudes can be seen in Fig. 4.14, where ϵ and i can be read respectively in the left and right vertical axis.

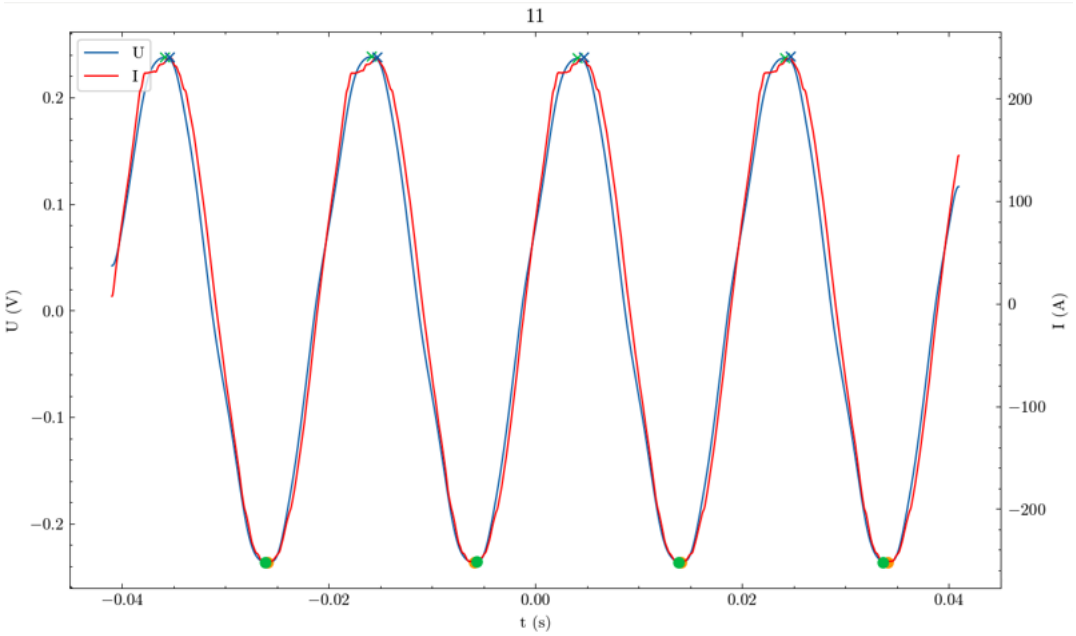

Figure 4.14: Time graph of electromotive force and current of sample I for the highest values of I_{AMP}

The average energy for each measurement can be seen in Fig. 4.15, with it's respective fit curve which is described by the equation $Q_{fit} = (5.33 \times 10^{-5})I^{2.9}$ with a fit quality of NRMSE= 0.067. This equation slightly deviates from the quadratic law function, as the value of β is not at all close to 2, proving that the sample's behavior is not ohmic.

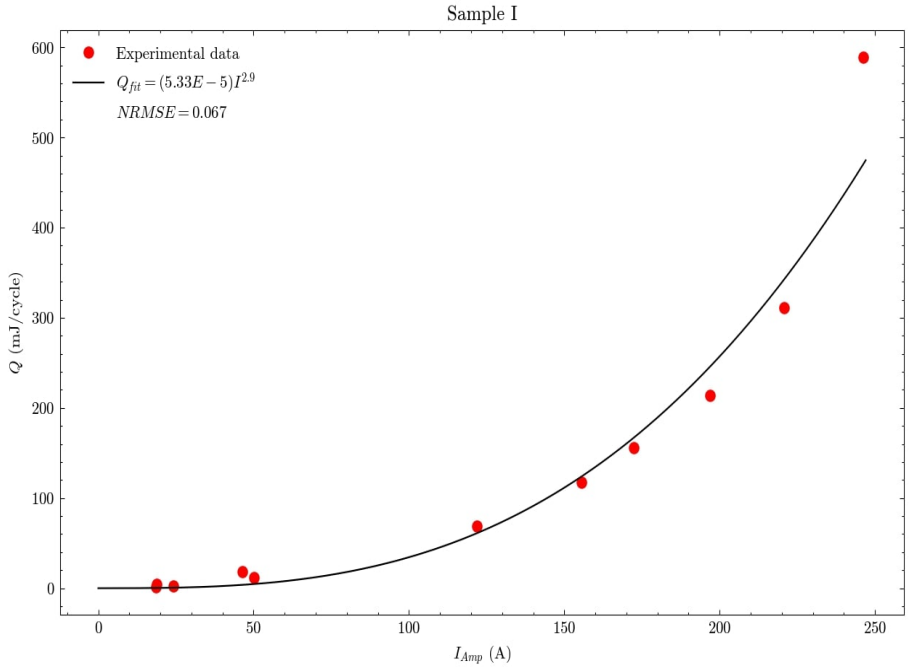

Figure 4.15: Graph of calculated average energies for single-phase sample I and respective power law fit curve in relation to current amplitude

4.3.1.2 Sample J

In this subsection are displayed the registered values while measuring the AC losses of the J sample, including its highest and lowest values of registered current and voltage, the calculated power losses and the average Impedance values of the tape.

In total, thirteen SQL files were taken during the experiment. The following figures show the registered values of the current, $I(A)$, and voltage, $U(V)$, for the highest and lowest values of current I_{AMP}. These results were registered within a time frame of $[-0.04; 0.04]$ seconds.

The average calculated phases between electromotive force, ϵ, and the induced current, i, throughout all data files, are close to 0° which shows the highly resistive nature of the winding sample J.The graph of the highest current amplitudes can be seen in Fig. 4.16, where ϵ and i can be read respectively in the left and right vertical axis.

The average energy for each measurement can be seen in Fig. 4.17, with it's respective fit curve which is described by the equation $Q_{fit} = (2.22 \times 10^{-3})I^{2.14}$ with a fit quality of NRMSE= 0.016. This equation is really similar to the power calculated by using Ohm's Law, RI^2, which proves that the sample's behavior is practically ohmic.

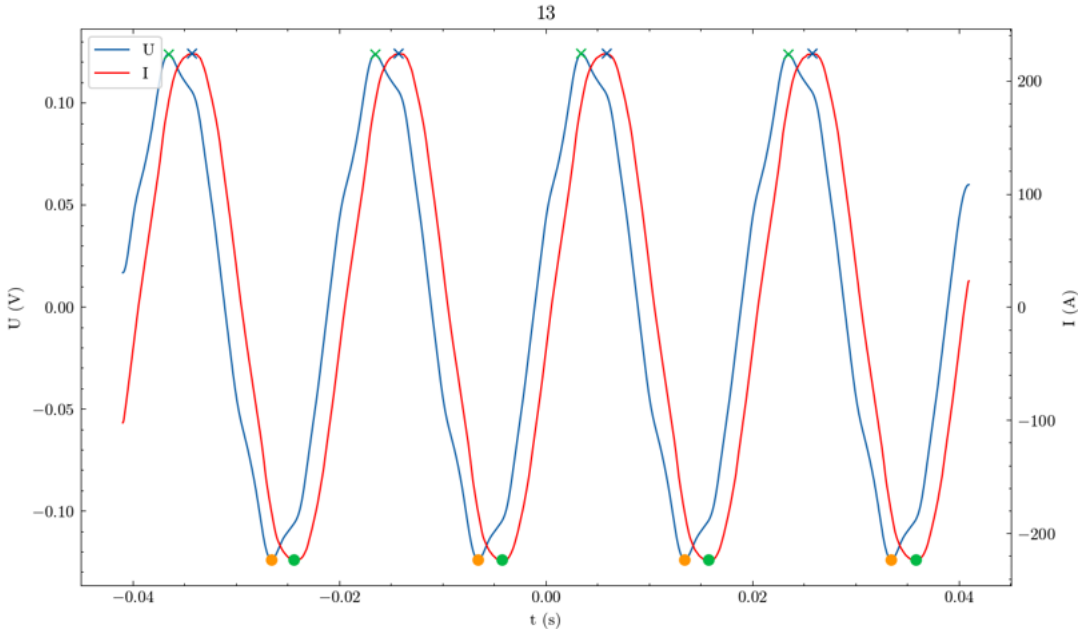

Figure 4.16: Time graph of electromotive force and current of sample J for the highest values of I_{AMP}

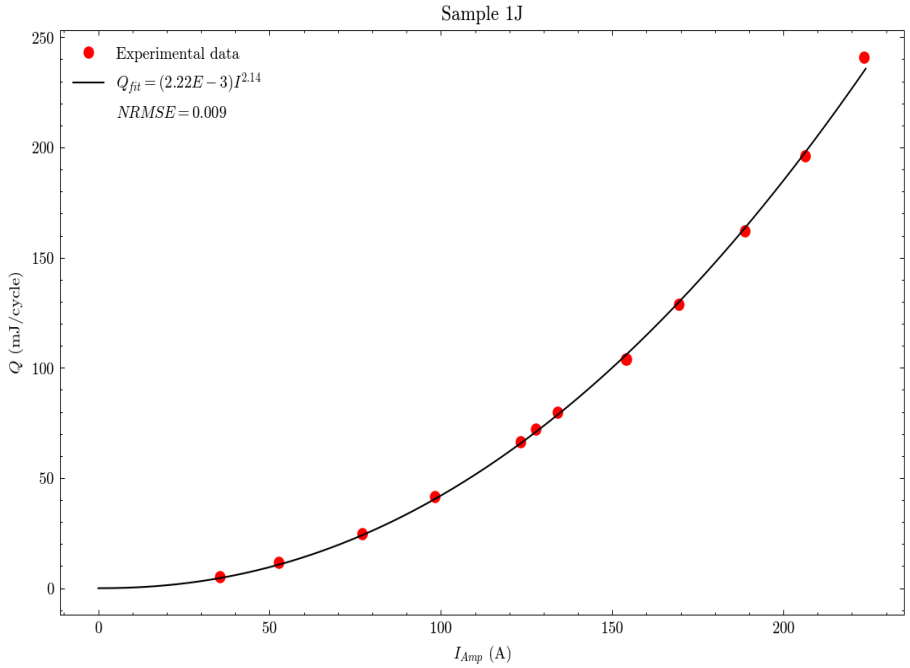

Figure 4.17: Graph of calculated average energies for single-phase sample J and respective power law fit curve in relation to current amplitude

Sample Name	α	β
Sample I	5.33×10^{-5}	2.90
Sample J	2.22×10^{-3}	2.14

Table 4.2: AC power losses of each sample, for windings with bridge-type joints.

4.3.1.3 Discussion

In the end we concluded, based on the results present in Table 4.2, that the power dissipation is different for each winding: As the sample J has a NRMSE value of 0.009, in contrast to sample I that has noticeable higher NRMSE value of 0.067. Which demonstrates that the Energy function of sample J fits much better into a power law function in contrast to sample I. Also their coefficients and exponents vary significantly, as both coefficients have different magnitudes (10^{-3} for J and 10^{-5} for sample I) and the exponents have a reasonable difference of 24% (2,22 and 2,9 for J and I respectively).

These deviations might be explained by the fact that sample J possesses a soldered area twice as big as the sample I which would explain the lower energy losses of sample I, just as expected. Although the fact that the NRMSE value of the sample I is higher than 5% may indicate that the sample might have lost its superconducting state just when it was injected with 250A of current, as the Energy loss had increased drastically in about a 25A difference as we can observe in figure.4.15.

4.3.2 Samples with lap-type joints

After obtaining the results for the previous samples, three more samples were created by Diogo Durão and Dr. Canan, but this time with lap-type joints. Each sample was made with same type of solder and using the same production method. This experiment was conducted to compare the losses of both types of joints and to understand their behavior may change when in a superconducting state.

The method used for this experiment is the same as the previous one for the bridge-type joints, but with the small difference that, with the new molds already created, the latest samples dubbed samples 1, 2, and 3 were placed inside the cryostats. The assembly of all devices used for this experiment is shown in the figure 4.18.

Figure 4.18: Assembly of all equipments for measuring the ac losses of the lap-type windings.

4.3.2.1 Sample 1

In this subsection are displayed the registered values while measuring the AC losses of sample 1, including its highest and lowest values of registered current and voltage, the calculated power losses and the average Impedance values of the tape.

In total, thirteen SQL files were taken during the experiment. The following figure shows the registered values of the current, $I(A)$, and voltage, $U(V)$, for the highest values of current I_{AMP}. These results were registered within a time frame of $[-0.08; 0.08]$ seconds.

Regardless of each primary, the average calculated phases between electromotive force, ϵ, and the induced current, i, throughout all data files, are close to 0° which shows the highly resistive nature of the winding sample 1. The graph of the highest current amplitudes, when using the 40 spiral primary, can be seen in Fig. 4.19, where ϵ and i read respectively in the left and right vertical axis.

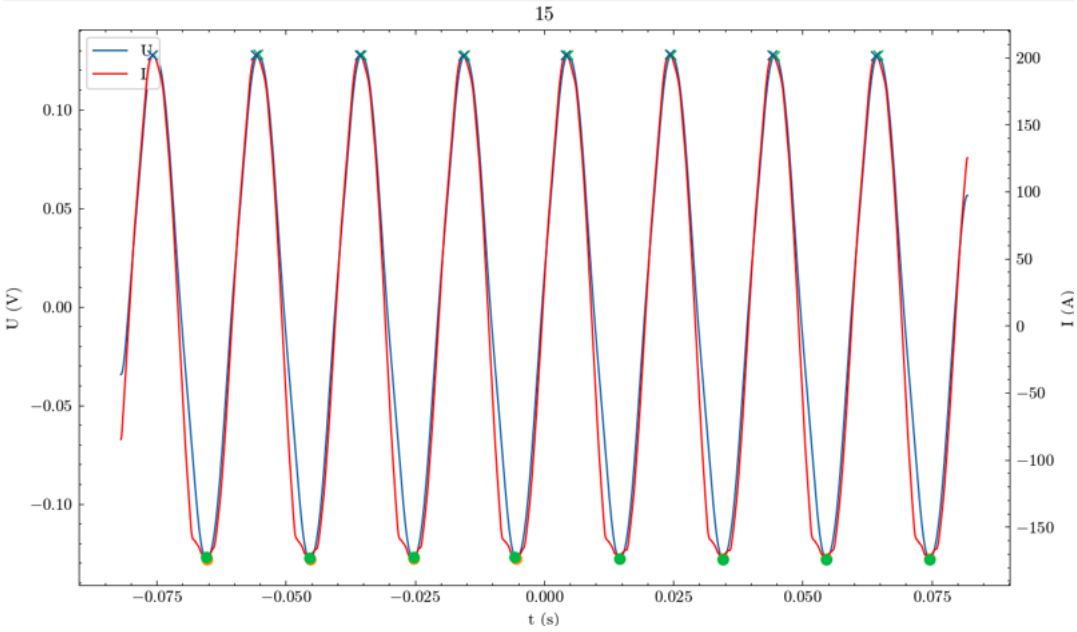

Figure 4.19: Time graph of electromotive force and current of sample 1 for the highest values of I_{AMP}.

The average energy for each measurement for both primaries can be seen in Fig.4.21. and Fig.4.20.(for 10 and 40 spirals, respectively); with it's respective fit curve which is described by the equations $Q_{fit} = (5.58 \times 10^{-3})I^{2.13}$ with a fit quality of NRMSE= 0.018 for the primary with 10 spirals and $Q_{fit} = (3.80 \times 10^{-3})I^{2.12}$ with a fit quality of NRMSE= 0.013 for the primary with 40 spirals. Both equation are really similar to the power calculated by using Ohm's Law, RI^2, which proves that the samples have a practically ohmic behavior.

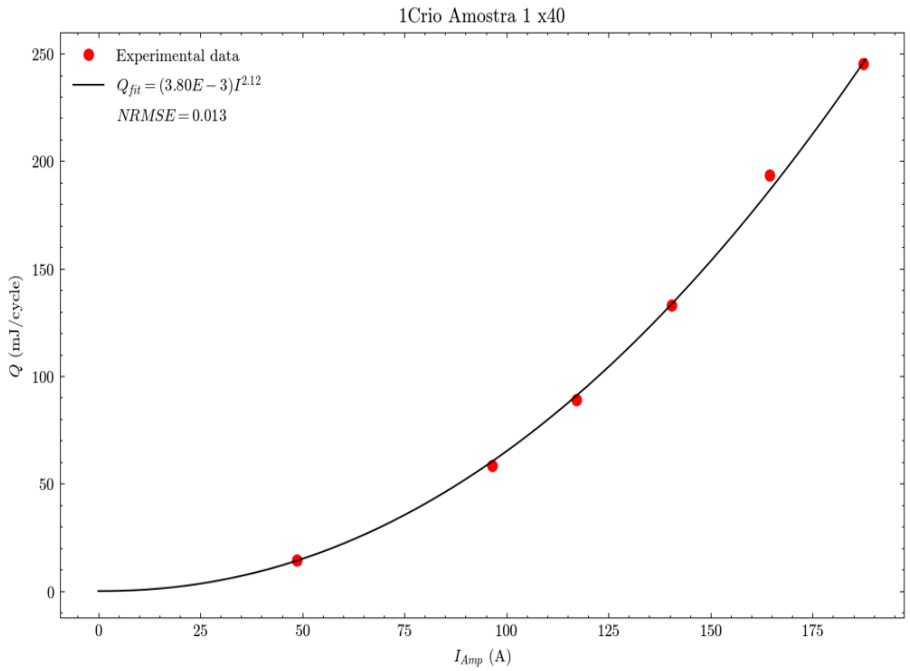

Figure 4.20: Graph of calculated average energies for single-phase sample 1 and respective power law fit curve in relation to current amplitude; when using a 40 spiral primary

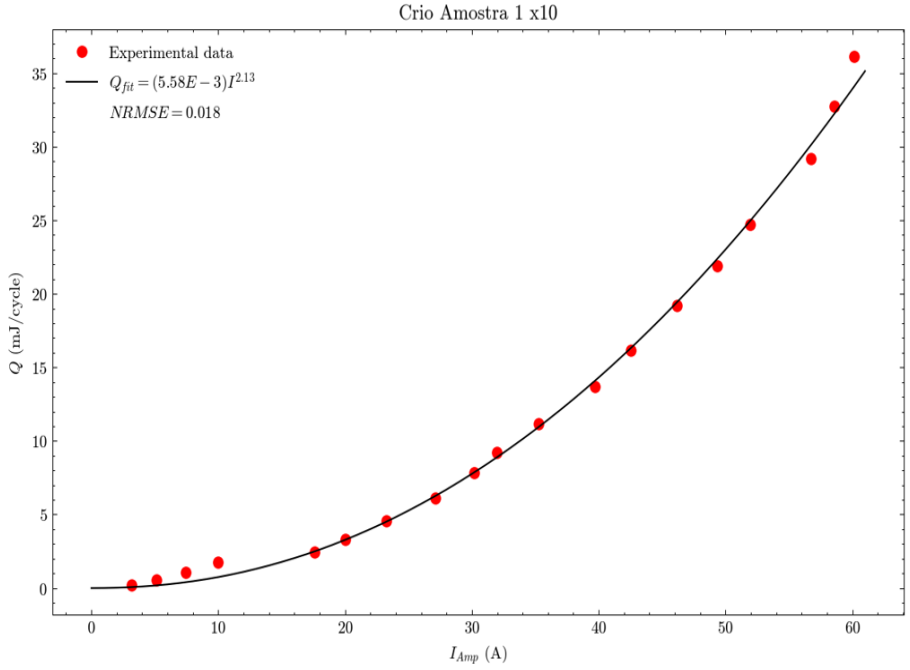

Figure 4.21: Graph of calculated average energies for single-phase sample 1 and respective power law fit curve in relation to current amplitude; when using a 10 spiral primary

4.3.2.2 Sample 2

In this subsection are displayed the registered values while measuring the AC losses of sample 2, including its highest and lowest values of registered current and voltage, the calculated power losses and the average Impedance values of the tape.

In total, thirteen SQL files were taken during the experiment. The following figure shows the registered values of the current, $I(A)$, and voltage, $U(V)$, for the highest of current I_{AMP}. These results were registered within a time frame of $[-0.08; 0.08]$ seconds.

Regardless of each primary, the calculated phases between electromotive force, ϵ, and the induced current, i, throughout all data files, are close to 0° which shows the highly resistive nature of the winding sample 2. The graph of highest current amplitudes, when using the 40 spiral primary, can be seen in Fig. 4.22, where ϵ and i can be read respectively in the left and right vertical axis.

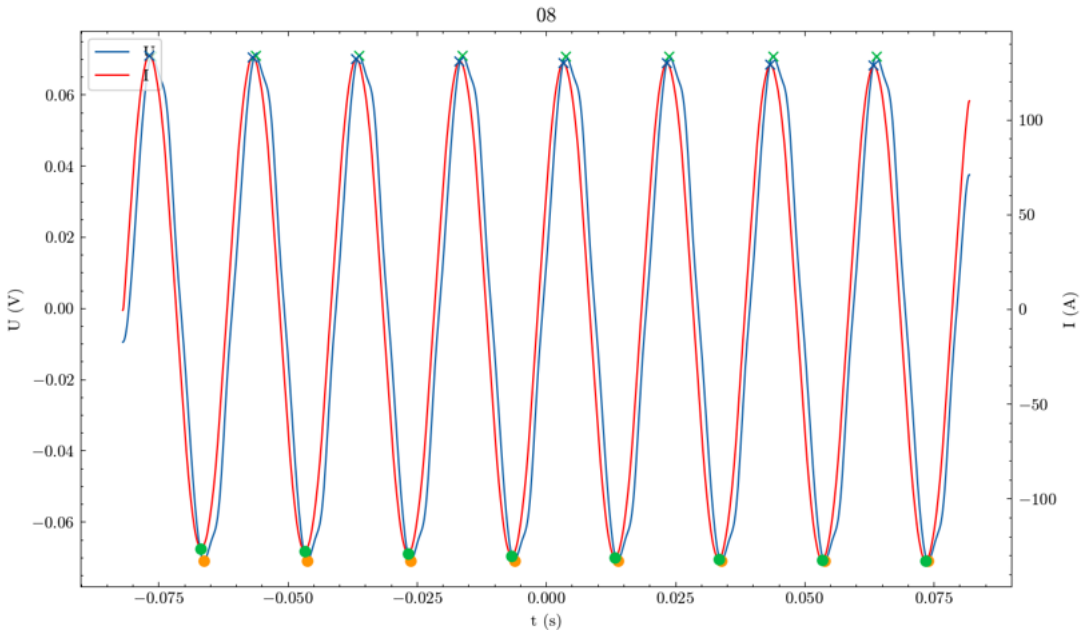

Figure 4.22: Time graph of electromotive force and current of sample 2 for the highest values of I_{AMP}.

The average energy for each measurement for both primaries can be seen in Fig 4.24 and Fig 4.23(for 10 and 40 spirals, respectively); with it's respective fit curve which is described by the equations $Q_{fit} = (1.34 \times 10^{-2})I^{1.95}$ with a fit quality of NRMSE= 0.005 for the primary with 10 spirals and $Q_{fit} = (9.04 \times 10^{-3})I^{1.89}$ with a fit quality of NRMSE= 0.009 for the primary with 40 spirals. Both equation are really similar to the power calculated by using Ohm's Law, RI^2, which proves that the samples have a practically ohmic behavior.

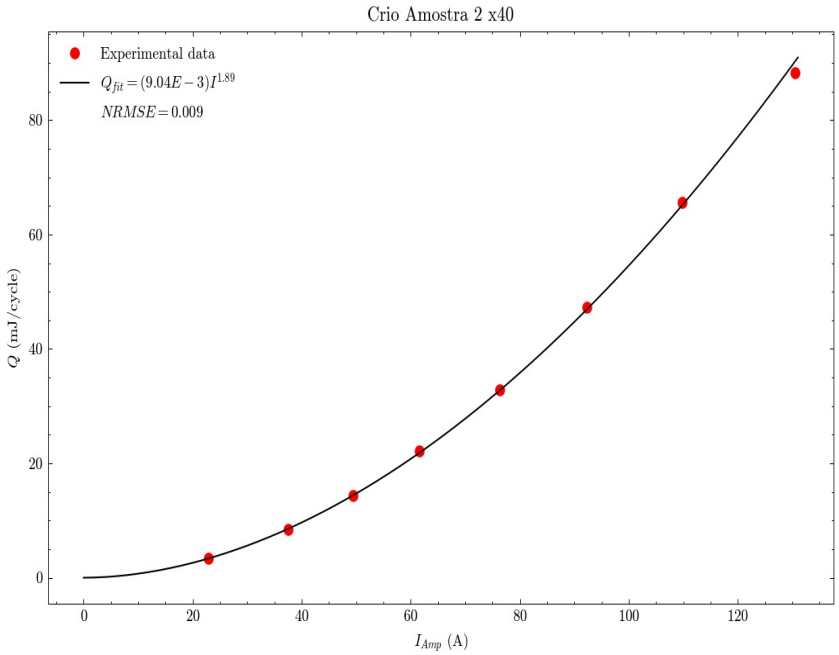

Figure 4.23: Graph of calculated average energies for single-phase sample 2 and respective power law fit curve in relation to current amplitude; when using a 40 spiral primary

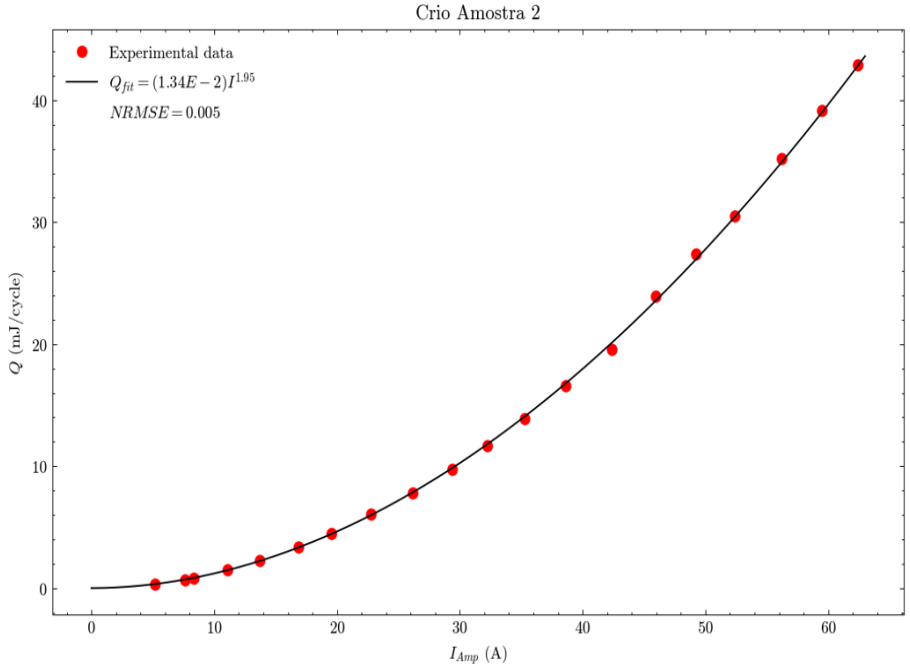

Figure 4.24: Graph of calculated average energies for single-phase sample 2 and respective power law fit curve in relation to current amplitude; when using a 10 spiral primary

4.3.2.3 Sample 3

In this subsection are displayed the registered values while measuring the AC losses of sample 3, including its highest and lowest values of registered current and voltage, the calculated power losses and the average Impedance values of the tape.

In total, thirteen SQL files were taken during the experiment. The following figure shows the registered values of the current, $I(A)$, and voltage, $U(V)$, for the highest values of current I_{AMP}. These results were registered within a time frame of $[-0.08; 0.08]$ seconds.

Regardless of each primary, the calculated phases between electromotive force, ϵ, and the induced current, i, throughout all data files, are bigger than 0° which shows this sample has a higher inductive nature than the other winding samples. The graph of the highest current amplitudes of I_{AMP}, when using the 40 spiral primary, can be seen in Fig.4.25, where ϵ and i can be read respectively in the left and right vertical axis.

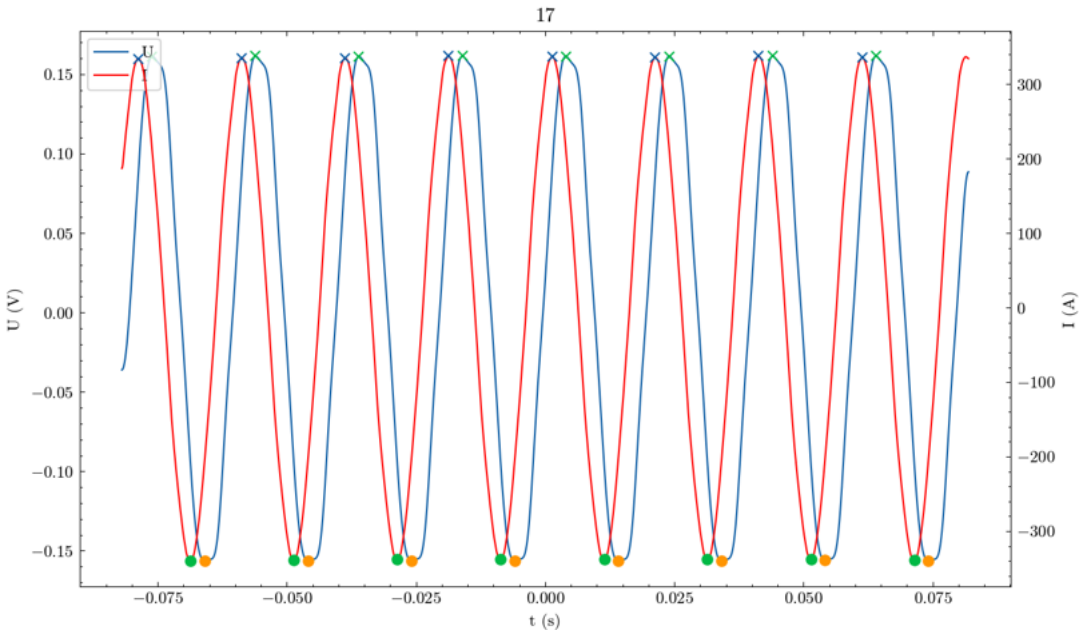

Figure 4.25: Time graph of electromotive force and current of sample 3 for the highest and lowest values of I_{AMP}.

The average energy for each measurement for both primaries can be seen in Fig 4.27 and Fig 4.26(for 10 and 40 spirals, respectively); with it's respective fit curve which is described by the equations $Q_{fit} = (2.07 \times 10^{-3})I^{2.03}$ with a fit quality of NRMSE= 0.007 for the primary with 10 spirals and $Q_{fit} = (1.75 \times 10^{-3})I^{2.07}$ with a fit quality of NRMSE= 0.009 for the primary with 40 spirals. Both equation are really similar to the power calculated by using Ohm's Law, RI^2, which proves that the samples have a practically ohmic behavior.

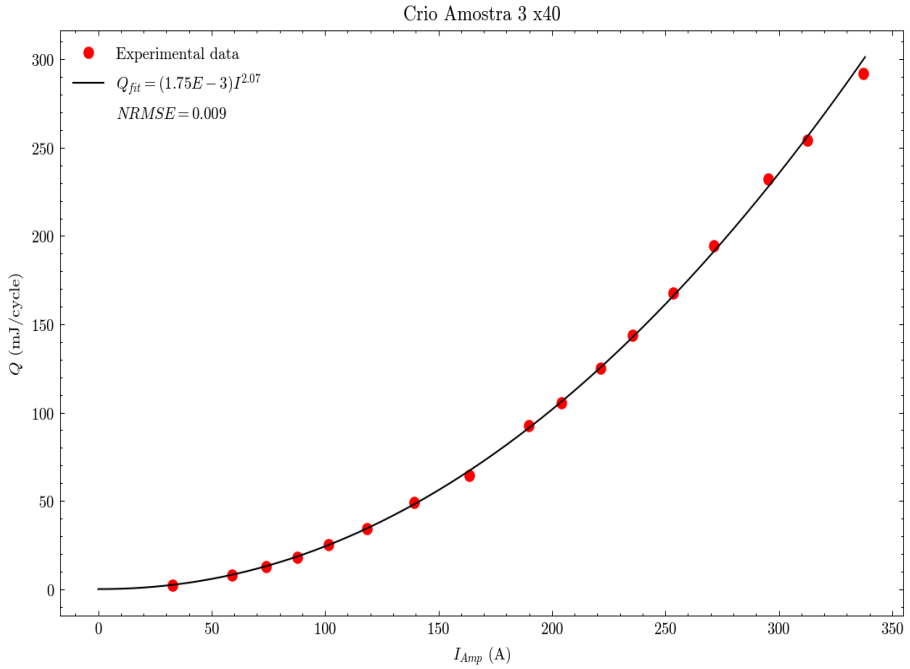

Figure 4.26: Graph of calculated average energies for single-phase sample 3 and respective power law fit curve in relation to current amplitude; when using a 40 spiral primary

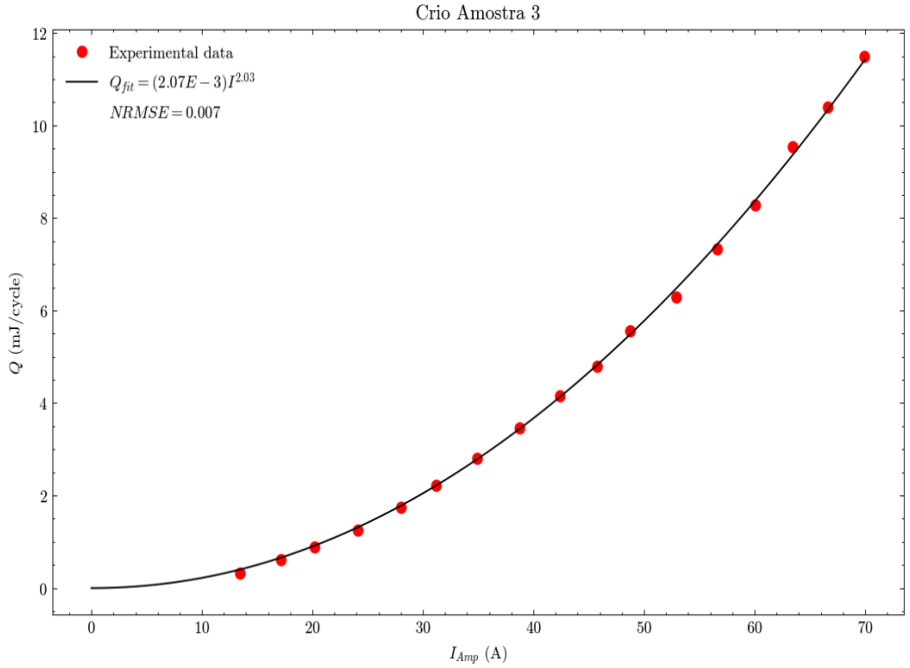

Figure 4.27: Graph of calculated average energies for single-phase sample 3 and respective power law fit curve in relation to current amplitude; when using a 10 spiral primary

Sample Name	Number of Spirals	α	β
Sample 1	10	5.58×10^{-3}	2.13
Sample 2	10	1.34×10^{-2}	1.95
Sample 3	10	2.07×10^{-3}	2.03
Sample 1	40	3.80×10^{-3}	2.12
Sample 2	40	9.04×10^{-3}	1.89
Sample 3	40	1.75×10^{-3}	2.07

Table 4.3: AC losses of each samples depending on the number of spirals of the primary.

4.3.2.4 Discussion

In the end we concluded, based on the results present in Table 4.3, that all the windings have an average energy function that fits reasonably well to a power law function (having NRMSE values below 0.05), and also all of them had exponents close to 2 which means that samples 1 and 2 exhibited a behavior that was practically ohmic, while sample 3 has a noticeable higher phase than the other samples, showing a more inductive behavior.

When using a 10 spirals primary, the values of the coefficients remained close to a magnitude of 10^{-3}, with sample 2 reaching the highest value of 1.34×10^{-2} while sample 3 reached the lowest value of 2.07×10^{-3}. When switching for a primary with 40 spirals, its important to note that samples 1 and 2 stopped being in a superconducting state at a I_{AMP} value of about 200A, while sample 3 persisted in a superconducting state until values close to 350A. This fact and the higher levels of phase maybe explained by imperfections or lack of precision in the soldering process method. One possibility may be the uneven spread of solder around the soldering area, as the higher concentrations of solder can result rise the R_{solder} in certain points that increase the energy losses and limit the range I_{AMP} that the sample remains in a superconducting state.

Nevertheless, this switch of primaries resulted in an overall decrease of the samples α; of about 32% for sample 1 and 2, while sample 3 only decreased 15% . The small decrease might be attributed to an overshoot error in the fitting process when using the primary winding with 10 spirals. The most reliable results are likely those obtained with the winding that has 40 spirals, as the samples used in this configuration have been subjected to a wider range of currents.

4.4 AC Experiments without using Iron Core

These last experiments were made with the objective to determine whether if the iron core of the SFCL and the distance between the two voltage conductors of the samples have any impact on the losses measured. Therefore, for each of the Lap-type Winding samples a second pair of conducting wires was added; both at a distance of 6cm from the center of the soldered area, and therefore, 12cm from each other. So it is expected that the measured u_v between 6cm to be twice as high comparatively to a distance of 12cm.

In addiction, instead of placing the samples inside of cryostats that were connected to the iron core of the SFCL, the samples were placed in a styrofoam box along with the previously used primary windings with 40 spirals. The samples were then positioned around the primaries at about half their height, then each pair of voltage conductors were connected to a circuit V that were linked to an oscilloscope with three input entries. The assembly of the samples used in this experiment is shown in the figure 4.28.

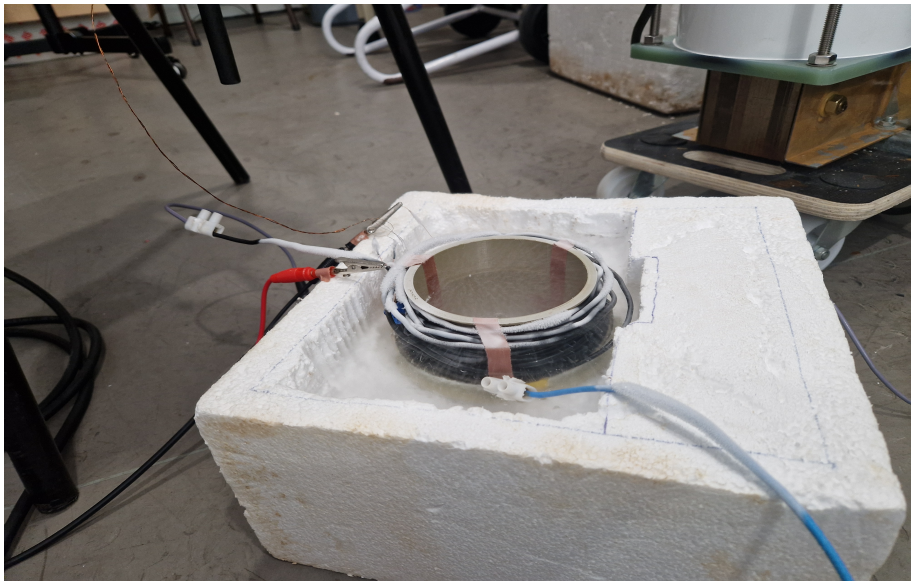

Figure 4.28: Assembly of the samples when not using the iron core of the SFCL.

4.4.0.1 Sample 1

In this subsection are displayed the registered values while measuring the AC losses of sample 1 without the use of the SFCL's iron core, including its highest and lowest values of registered current and voltage, the calculated power losses and the average Impedance values of the tape. Where the measured u_v between two points 12cm apart is displayed in channel 1, while the measured u_v between a distance of 6cm is displayed in channel 2.

In total, nineteen SQL files were taken during the experiment. The following figures show the registered values of the current, $I(A)$, and voltage, $U(V)$, for the highest and lowest values of current I_{AMP}. These results were registered within a time frame of $[-0.00; 0.07]$ seconds.

The following Figures 4.29 and 4.30, show the registered voltage of the sample for the highest amount of I_{AMP}.

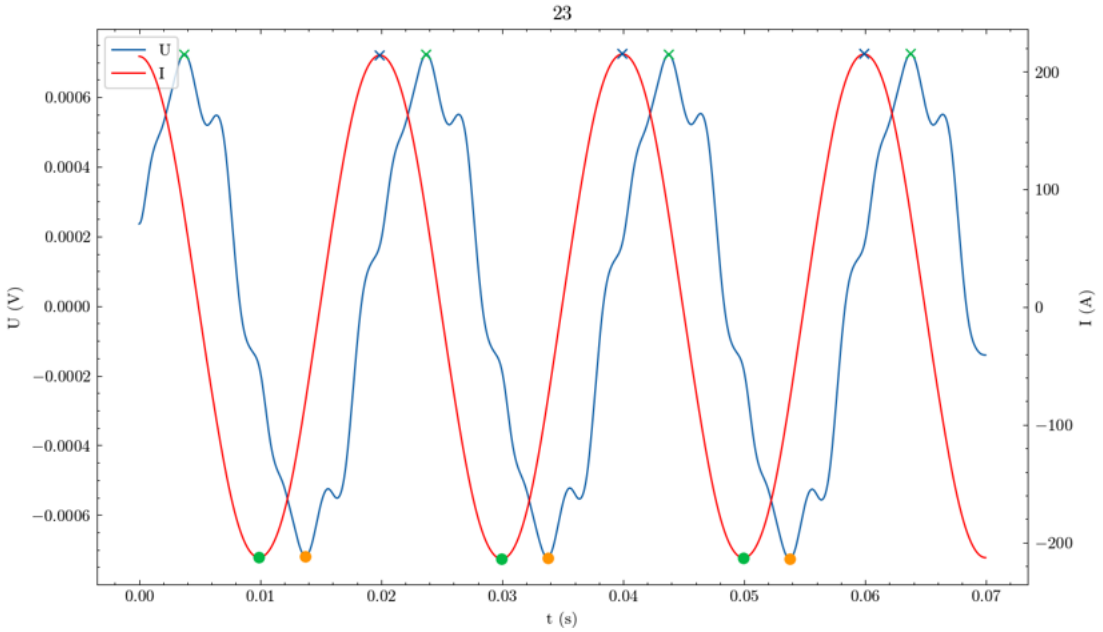

Figure 4.29: Time graph of electromotive force and current of sample 1 for the highest values of I_{AMP} and for a distance of 12cm.

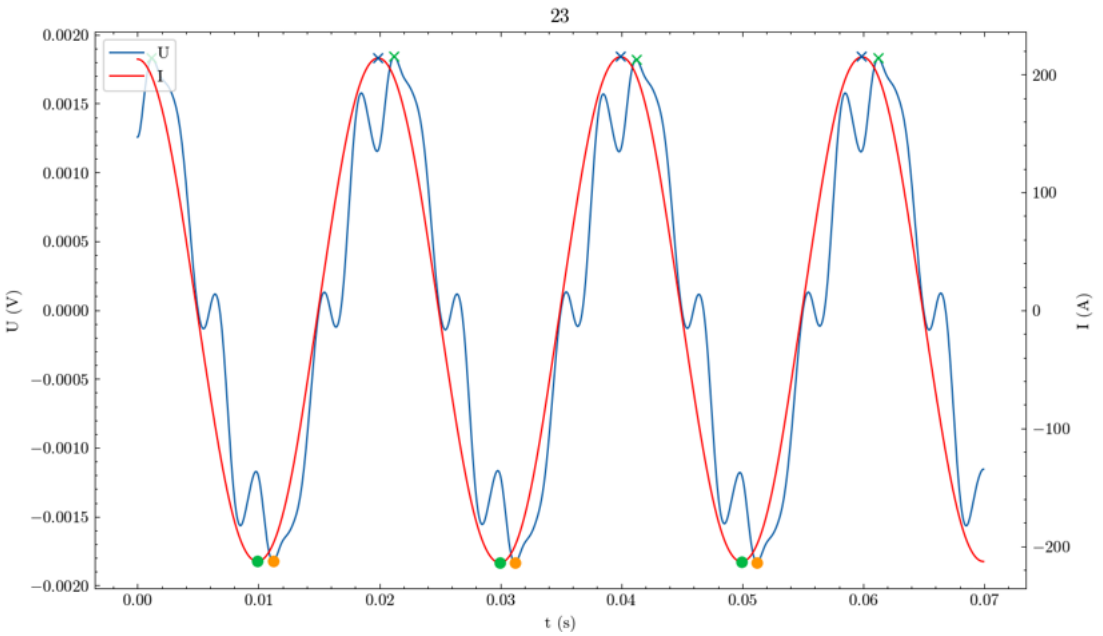

Figure 4.30: Time graph of electromotive force and current of sample 1 for the highest values of I_{AMP} and for a distance of 6cm.

From these registered values we can conclude that the voltage between the closest distancing wires (6cm, in channel 2) is significantly higher (About 3.1 times higher) than the voltage between the wires that have twice the distance distancing wires (12cm, in channel 1). We can also observe that the phase between the electromotive force, ϵ, and

the induced current, i, is significantly higher among the values in channel 1 than channel 2. This means that the sample has a more inductive behavior when measuring from two points the farther away they are.

The average energy for each measurement in Channel 2 (6cm) can be seen in Fig.4.31, with it's respective fit curve which is described by the equation $Q_{fit} = (3.46 \times 10^{-5})I^{1.79}$ with a fit quality of NRMSE= 0.022. This equation is not similar to the power calculated by using Ohm's Law, RI^2, which shows that the sample's behaviour is not ohmic.

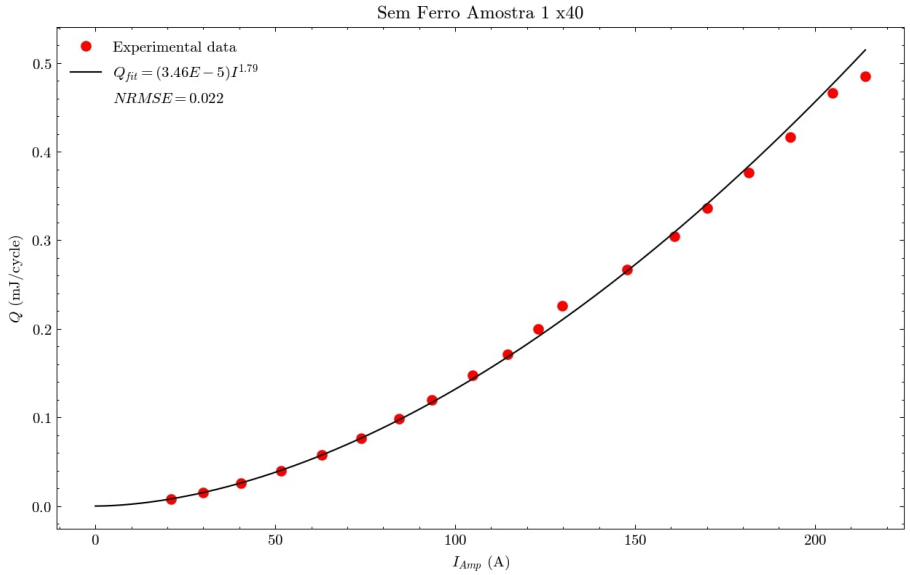

Figure 4.31: Graph of calculated average energies for single-phase sample 1 and respective power law fit curve in relation to current amplitude

4.4.0.2 Sample 2

In this subsection are displayed the registered values while measuring the AC losses of sample 2 without the use of the SFCL's iron core, including its highest and lowest values of registered current and voltage, the calculated power losses and the average Impedance values of the tape. Where the measured u_v between two points 12cm apart is displayed in channel 1, while the measured u_v between a distance of 6cm is displayed in channel 2.

In total, twenty one SQL files were taken during the experiment. The following figures show the registered values of the current, $I(A)$, and voltage, $U(V)$, for the highest and lowest values of current I_{AMP}. These results were registered within a time frame of $[-0.00; 0.07]$ seconds.

The following Figures 4.32 and 4.33 show the registered voltage of the sample for the highest amount of I_{AMP}.

From these registered values we can conclude that the voltage between the closest distancing wires (6cm, in channel 2) is significantly higher (about 4.4 times higher) than the voltage between the wires that have twice the distance distancing wires (12cm, in channel 1). We can also observe that the phase between the electromotive force, ϵ, and the

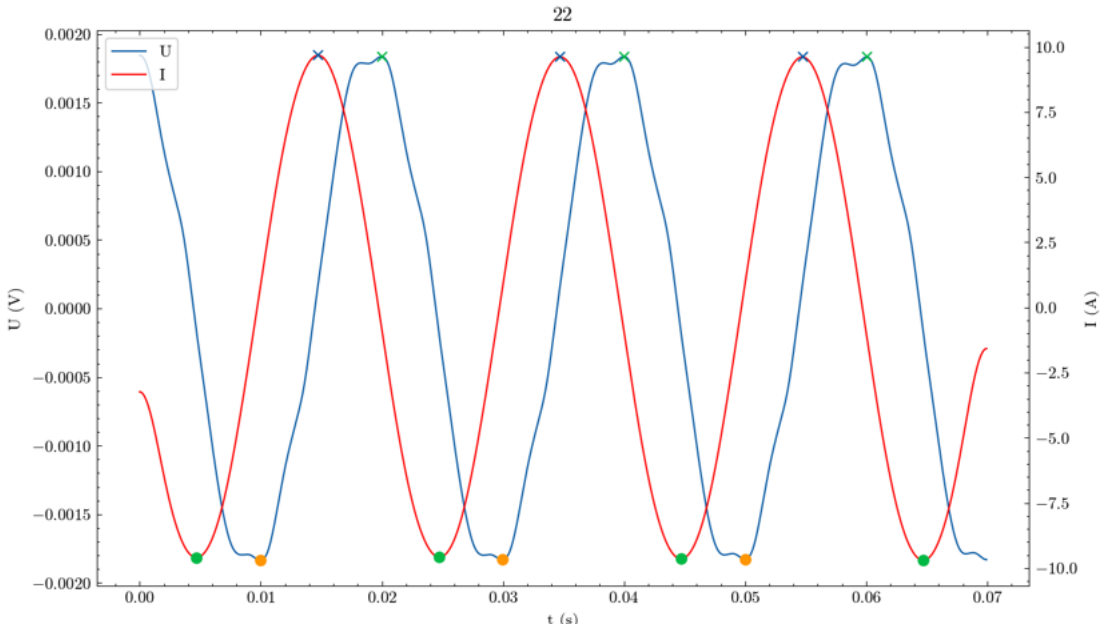

Figure 4.32: Time graph of electromotive force and current of sample 2 for the highest values of I_{AMP} and for a distance of 12cm.

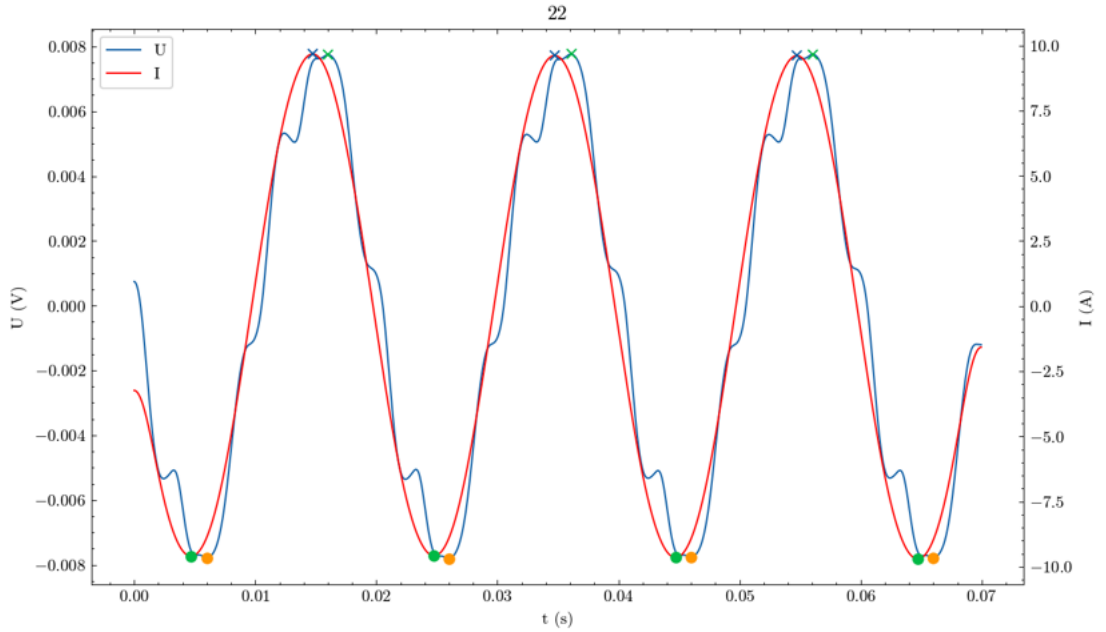

Figure 4.33: Time graph of electromotive force and current of sample 2 for the highest values of I_{AMP} and for a distance of 6cm.

induced current, i, is significantly higher among the values in channel 1 than channel 2. This too means that the sample has a more inductive behavior when measuring from two points the farther away they are.

The average energy for each measurement in Channel 2 (6cm) can be seen in Fig. 4.34, with it's respective fit curve which is described by the equation $Q_{fit} = (9.75 \times 10^{-7})I^{2.47}$ with a fit quality of NRMSE= 0.018. This equation is not similar to the power calculated by using Ohm's Law, RI^2, which shows that the sample's behavior is not ohmic.

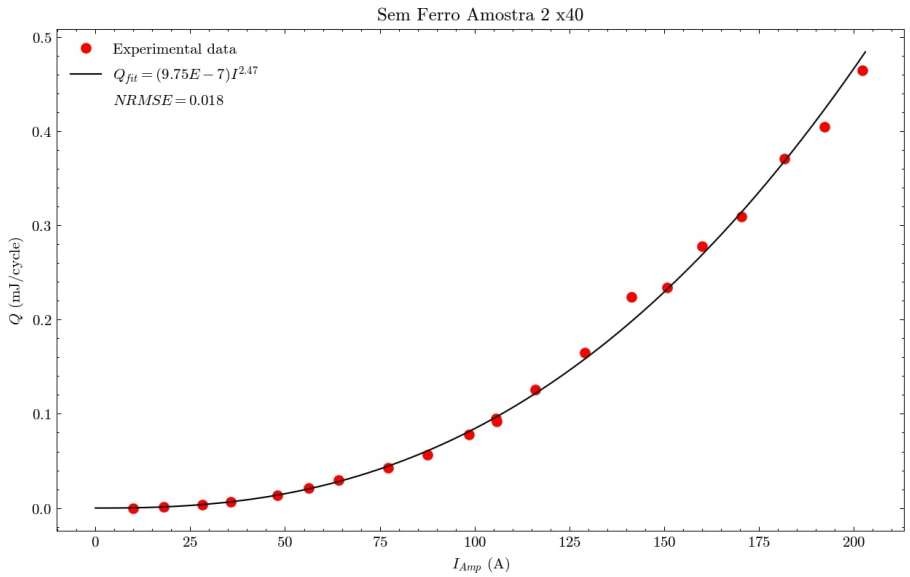

Figure 4.34: Graph of calculated average energies for single-phase sample 2 and respective power law fit curve in relation to current amplitude

4.4.0.3 Sample 3

In this subsection are displayed the registered values while measuring the AC losses of sample 3 without the use of the SFCL's iron core, including its highest and lowest values of registered current and voltage, the calculated power losses and the average Impedance values of the tape. Where the measured u_v between two points 12cm apart is displayed in channel 1, while the measured u_v between a distance of 6cm is displayed in channel 2.

In total, sixteen SQL files were taken during the experiment. The following figures show the registered values of the current, $I(A)$, and voltage, $U(V)$, for the highest and lowest values of current I_{AMP}. These results were registered within a time frame of $[-0.00; 0.07]$ seconds.

The following Figures 4.35 and 4.36, show the registered voltage of the sample for the highest amount of I_{AMP}.

From these registered values we can conclude that the voltage between the closest distancing wires (6cm, in channel 2) is significantly higher (About 5.1 times higher) than the voltage between the wires that have twice the distance distancing wires (12cm, in channel 1). We can also observe that the phase between the electromotive force, ϵ, and

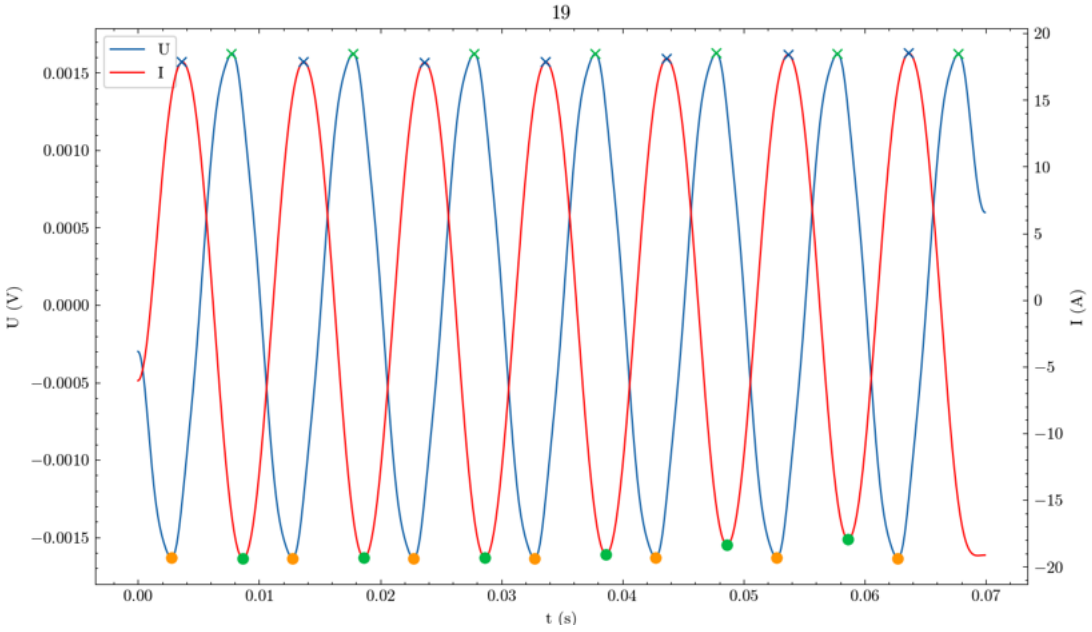

Figure 4.35: Time graph of electromotive force and current of sample 3 for the highest values of I_{AMP} and for a distance of 12cm.

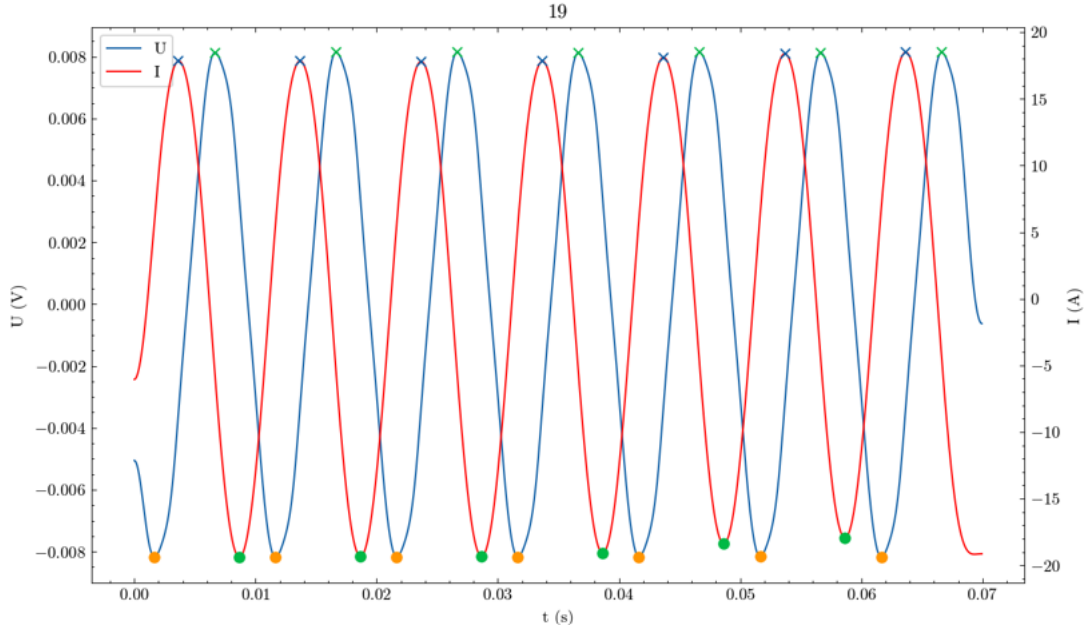

Figure 4.36: Time graph of electromotive force and current of sample 3 for the highest values of I_{AMP} and for a distance of 6cm.

the induced current, i, is slightly higher among the values in channel 1 than channel 2. This means, just like in the other samples, that this sample has a more inductive behavior when measuring from two points the farther away they are.

The average energy for each measurement in Channel 2 (6cm), can be seen in Fig. 4.37, with it's respective fit curve which is described by the equation $Q_{fit} = (7.21 \times 10^{-6})I^{2.28}$ with a fit quality of NRMSE= 0.012. This equation is not similar to the power calculated by using Ohm's Law, RI^2, which shows that the sample's behavior is not ohmic.

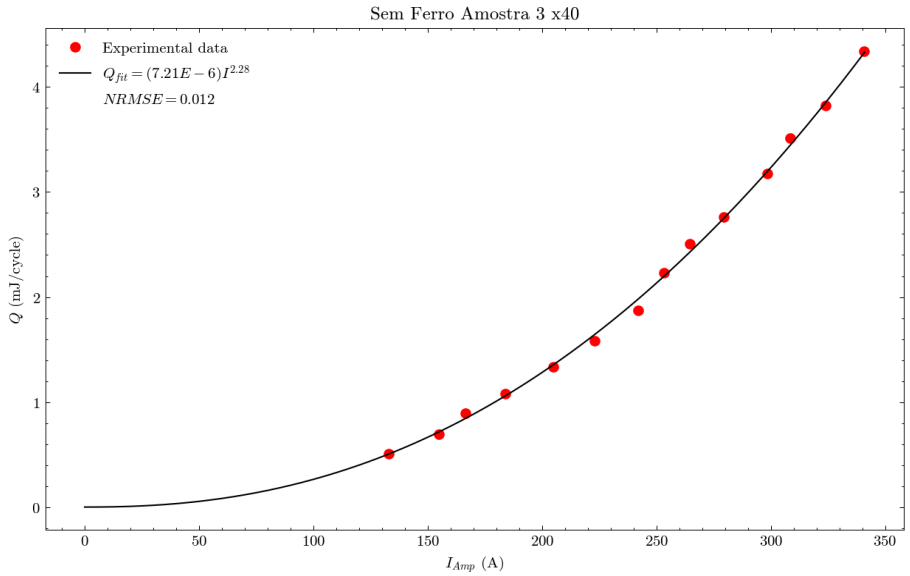

Figure 4.37: Graph of calculated average energies for single-phase sample 3 and respective power law fit curve in relation to current amplitude.

Sample Name	α	β
Sample 1	3.46×10^{-5}	1.96
Sample 2	9.75×10^{-7}	2.47
Sample 3	7.21×10^{-6}	2.28

Table 4.4: AC power losses of each sample, without using the iron core.

Types of Samples	Using SFCL	Spirals	Samples	α	β	Joint Type
Tape	No	-	Sample E	1.07×10^{-3}	1.96	Bridge
Tape	No	-	Sample G	1.04×10^{-3}	1.98	Bridge
Tape	No	-	Sample H	5.13×10^{-4}	2.05	Bridge
Winding	Yes	40	Sample I	5.33×10^{-5}	2.9	Bridge
Winding	Yes	40	Sample J	2.22×10^{-3}	2.14	Bridge
Winding	Yes	10	Sample 1	5.58×10^{-3}	2.13	Lap
Winding	Yes	10	Sample 2	1.34×10^{-2}	1.95	Lap
Winding	Yes	10	Sample 3	2.07×10^{-3}	2.03	Lap
Winding	Yes	40	Sample 1	3.80×10^{-3}	2.12	Lap
Winding	Yes	40	Sample 2	9.04×10^{-3}	1.89	Lap
Winding	Yes	40	Sample 3	1.75×10^{-3}	2.07	Lap
Winding	No	40	Sample 1	3.46×10^{-5}	1.79	Lap
Winding	No	40	Sample 2	9.75×10^{-7}	2.47	Lap
Winding	No	40	Sample 3	7.21×10^{-6}	2.28	Lap

Table 4.5: Registered AC losses of all the samples, for all experiments made.

4.4.1 Discussion

In the end we concluded, based on the registered values present in Table 4.4, that all the windings have an average energy function that fits reasonably well to a power law function (having NRMSE values below 0.05), with the β values varied between 1.79 to 2.47. The values of the coefficients had reached a vary array of magnitudes (10^{-5}, 10^{-7}, 10^{-6} for samples 1, 2 and 3 respectively), with sample 1 reaching the highest value of 3.46×10^{-5} while sample 2 reached the lowest value of 9.75×10^{-7}. There has been a significant decrease in the overall energy losses of the samples when comparing to using a SFCL, which is due to the absence of the iron core of the SFCL, as its presence would increase the current density that would be applied to each sample and therefore a decrease of energy losses comparing to when using a SFCL is expected.

It is important to note that, in all the experiments, the voltage is significantly decreases when measuring from twos wires with twice the original distance. Also each sample has a higher inductive behavior the farther away the conducting wires are from each other as the phase in channel 1 is always more than twice the values obtained in channel 2. Which means that the previously used method for measuring AC Losses is not totally viable.

The following Table 4.5 contains all the power loss results for all the experiments made in this project.

5

Conclusion

This dissertation aimed to measure the AC losses of an inductive transformer type SFCL, caused by balanced system losses, by calculating the electromotive force induction and current present in the secondary HTS windings of the SFCL. The objective was to better understand how the characteristics of soldered HTS windings influence power losses when integrated into a SFCL. These experiments will help us optimize the use of SFCL and minimize their energy losses, which is crucial for the overall electrification of energy systems.

This objective was successfully achieved through a Python program capable of analyzing the measured results through multiple electronic circuits that amplify, integrate and the current and voltage signals, coming through the SFCL. These signals were measured thanks to the creation of multiple practical instruments such as: rogowski coils that measured the current of the HTS windings, PLA supports that avoided mechanical damages to the winding samples and maintained a circular shape, new mechanical supports for measuring the solder resistance of HTS tapes, and some necessary upgrades to the already existing equipments. In the end, then we have acquired a better knowledge of how the many characteristics of soldered HTS samples can affect the AC energy Losses, in different scenarios, with or without using a SFCL operating in a monofasic phase. The registered values of the power losses ($Q = \alpha I_{Amp}^{\beta}$) for every sample in all the experiments are shown in Table 4.5.

In summary, the experiments on both lap-type and bridge-type joints, with and without the iron core of the SFCL, revealed key insights into the energy dissipation behavior of the windings.

When measuring the solder resistance of HTS tapes with bridge-type joints we reached the conclusion that some solder types materials offer a smaller resistance than others, depending on if the samples are being injected with DC current or AC current.

For the lap-type joints used along with the SFCL the iron core, all windings indicated a power behavior of the windings approximates well to power functions; with their coefficients remaining at close magnitudes, ranging from 10^{-2} to 10^{-3}, and their exponents close to 2, which concluded that each sample exhibited nearly ohmic behavior. It was also

apparent that one sample (sample 3) is able to maintain its superconducting state when injected to levels current higher than 200A when switching the primaries of the SFCL from 10 spirals to 40.

When the same samples were detached from the SFCL (and its iron core), it caused a reduction in β values of all the samples, though α values remained consistent and their functions resembling well the behavior of power functions. This decrease can be attributed to the absence of the SFCLs iron core, which typically increases current density that is being induced by the primary resulting in higher energy losses. But this decrease was not constant for all samples (9.11×10^{-3} lower for sample 1, 1.08×10^{-4} lower for sample 2, and 4.12×10^{-3} lower for sample 3). Revealing how the short-circuited HTS winding production is a very important step to ensure that these samples behave as ideally as possible.

For the bridge-type joints, it was concluded that the higher soldered area of a sample is, the higher will be the following power losses and the more likely it is for the sample to lose its superconducting state for high amounts of AC current. As the power dissipation varied across samples, with sample J demonstrating a much better fit to a power law than the other sample I which suggests that it may have lost its superconducting state at around 250 A. The exponents of each sample were also differed, with a difference of 24%.

In the last experiment it was also made aware that the original method for measuring AC losses is flawed as the ϵ changes according to the distance of the conducting points of the HTS samples, although we measured the AC losses for every sample with its soldered conducting wires at a constant distance of each other, they may not resemble the true ϵ value of the sample.

In the future, I hope some new experiments are made with the aim of measuring the AC losses of the HTS windings in multiple surface points to perfect the measuring method that is consistent with the obtained results. There should be a further inspection to the soldering method, in order to find a way to consistently replicate near identical samples, specially by creating a more meticulous way of spreading the soldering paste along the jointing area.

Overall, these findings highlight the strong impact of both the winding configuration and the presence of an iron core on energy dissipation and superconductivity. It also gave a better knowledge of how the differences in joint construction further influence the behavior of the windings and the impacts they have on the energy power losses when incorporated into superconducting fault current limiters.

Bibliography

[1] M. Q. Duong et al. "The impacts of distributed generation penetration into the power system". In: *2017 International Conference on Electromechanical and Power Systems (SIELMEN)*. 2017, pp. 295–301. DOI: 10.1109/SIELMEN.2017.8123336 (cit. on p. 1).

[2] L. Chen et al. "Application and Design of a Resistive-Type Superconducting Fault Current Limiter for Efficient Protection of a DC Microgrid". In: *IEEE Transactions on Applied Superconductivity* 29.2 (2019), pp. 1–7. DOI: 10.1109/TASC.2018.2882228 (cit. on p. 1).

[3] G. Gonçalves Sotelo et al. "A review of superconducting fault current limiters compared with other proven technologies". In: *Superconductivity* 3 (2022), p. 100018. ISSN: 2772-8307. DOI: https://doi.org/10.1016/j.supcon.2022.100018. URL: https://www.sciencedirect.com/science/article/pii/S2772830722000175 (cit. on p. 1).

[4] J. T. Kephart et al. "High Temperature Superconducting Degaussing From Feasibility Study to Fleet Adoption". In: *IEEE Transactions on Applied Superconductivity* 21.3 (2011), pp. 2229–2232. DOI: 10.1109/TASC.2010.2092746 (cit. on p. 2).

[5] J. F. Maguire et al. "Progress and Status of a 2G HTS Power Cable to Be Installed in the Long Island Power Authority (LIPA) Grid". In: *IEEE Transactions on Applied Superconductivity* 21.3 (2011), pp. 961–966. DOI: 10.1109/TASC.2010.2093108 (cit. on p. 2).

[6] R. Reed. "Trends and Advances in Cryogenic Materials". In: *Cryogenic Engineering*. Ed. by K. D. Timmerhaus and R. P. Reed. New York, NY: Springer New York, 2007. DOI: 10.1007/0-387-46896-X_3. URL: https://doi.org/10.1007/0-387-46896-X_3 (cit. on p. 2).

[7] D. Durão, J. Murta-Pina, and I. Catarino. "Superconductivity for energy applications Impact of Unbalanced Loads on AC Losses of Inductive HTS Fault Current Limiters". In: (2023), p. 69. URL: http://hdl.handle.net/10362/163752 (cit. on pp. 2, 14–16, 21, 24–26, 28, 69).

[8] D. Durão, J. Murta-Pina, and I. Catarino. "Impact of Unbalanced Loads on the AC Losses of Inductive HTS Fault Current Limiters". In: *IEEE Transactions on Applied Superconductivity* 34.3 (2024), pp. 1–4. DOI: 10.1109/TASC.2024.3353699 (cit. on p. 2).

[9] T. Janowski et al. "Properties comparison of superconducting fault current limiters with closed and open core". In: *IEEE Transactions on Applied Superconductivity* 13.2 (2003), pp. 2072–2075. DOI: 10.1109/TASC.2003.812991 (cit. on p. 3).

[10] V. Kozhevnikov. "Electrodynamics of superconductors". In: *Encyclopedia of Condensed Matter Physics (Second Edition)*. Ed. by T. Chakraborty. Second Edition. Oxford: Academic Press, 2024, pp. 644–656. ISBN: 978-0-323-91408-6. DOI: https://doi.org/10.1016/B978-0-323-90800-9.00036-6. URL: https://www.sciencedirect.com/science/article/pii/B9780323908009000366 (cit. on p. 5).

[11] A. Bussmann-Holder and H. Keller. "High-temperature superconductors: underlying physics and applications". In: *Zeitschrift für Naturforschung B* 75.1-2 (2020), pp. 3–14. DOI: doi:10.1515/znb-2019-0103. URL: https://doi.org/10.1515/znb-2019-0103 (cit. on pp. 5, 6).

[12] M. Tinkham. *Introduction to Superconductivity*. Dover Books on Physics Series. Dover Publications, 2004. ISBN: 9780486134727. URL: https://books.google.pt/books?id=VpUk3NfwDIkC (cit. on p. 6).

[13] K. A. Müller. "On the superconductivity in hole doped cuprates". In: *Journal of Physics: Condensed Matter* 19.25 (2007). DOI: 10.1088/0953-8984/19/25/251002. URL: https://dx.doi.org/10.1088/0953-8984/19/25/251002 (cit. on p. 6).

[14] W. V. Hassenzahl et al. "Electric power applications of superconductivity". In: *Proceedings of the IEEE* 92.10 (2004), pp. 1655–1674 (cit. on p. 7).

[15] H. Zhang et al. "Alternating Current Loss of Superconductors Applied to Superconducting Electrical Machines". In: *Energies* 14.8 (2021). ISSN: 1996-1073. DOI: 10.3390/en14082234. URL: https://www.mdpi.com/1996-1073/14/8/2234 (cit. on p. 7).

[16] O. of Electricity Delivery and U. D. o. E. Energy Reliability. "fault-current-limiters-fcl-fact-sheet". In: (). URL: https://www.energy.gov/oe/articles/fault-current-limiters-fcl-fact-sheet (cit. on p. 8).

[17] W.-J. Park, B. C. Sung, and J.-W. Park. "The Effect of SFCL on Electric Power Grid With Wind-Turbine Generation System". In: *IEEE Transactions on Applied Superconductivity* 20.3 (2010), pp. 1177–1181. DOI: 10.1109/TASC.2010.2040918 (cit. on p. 8).

[18] Y. Shirai et al. "Enhancement Test of Critical Clearing Time of One-Machine Infinite Bus Transmission System by Use of SFCL". In: *IEEE Transactions on Applied Superconductivity* 28.4 (2018), pp. 1–5. DOI: 10.1109/TASC.2018.2796628 (cit. on p. 8).

[19] S. Hemmati and J. Sadeh. "Applying superconductive fault current limiter to minimize the impacts of distributed generation on the distribution protection systems". In: *2012 11th International Conference on Environment and Electrical Engineering*. IEEE. 2012, pp. 808–813 (cit. on p. 8).

[20] M. S. Alam, M. A. Y. Abido, and I. El-Amin. "Fault Current Limiters in Power Systems: A Comprehensive Review". In: *Energies* 11.5 (2018). ISSN: 1996-1073. DOI: 10.3390/en11051025. URL: https://www.mdpi.com/1996-1073/11/5/1025 (cit. on p. 9).

[21] M. Noe and M. Steurer. "High-temperature superconductor fault current limiters: concepts, applications, and development status". In: *Superconductor Science and Technology* 20.3 (2007), R15. DOI: 10.1088/0953-2048/20/3/R01. URL: https://dx.doi.org/10.1088/0953-2048/20/3/R01 (cit. on p. 9).

[22] S. Kalia. "Cryogenic processing: a study of materials at low temperatures". In: *Journal of Low Temperature Physics* 158.5-6 (2010), pp. 934–945 (cit. on p. 10).

[23] V Parma. *Cryostat Design*. en. 2014. DOI: 10.5170/CERN-2014-005.353. URL: http://cds.cern.ch/record/1974062 (cit. on p. 11).

[24] M. H. Samimi et al. "The Rogowski Coil Principles and Applications: A Review". In: *IEEE Sensors Journal* 15.2 (2015), pp. 651–658. DOI: 10.1109/JSEN.2014.2362940 (cit. on p. 12).

[25] Y. Jun et al. "Design of a flexible rogowski coil with active integrator applied in lightning current collection". In: *2016 33rd International Conference on Lightning Protection (ICLP)*. 2016, pp. 1–7. DOI: 10.1109/ICLP.2016.7791472 (cit. on p. 13).

[26] H. Kondo et al. "Evaluation of superconducting coil for microwave power transmission". In: *2016 IEEE Region 10 Conference (TENCON)*. 2016, pp. 739–742. DOI: 10.1109/TENCON.2016.7848101 (cit. on p. 13).

[27] T. D. GmbH. "Pro-Line Product Overview". In: (October 2019). URL: https://www.theva.de/en/wp-content/uploads/sites/3/2019/10/TPL_Overview_10-2019.pdf (cit. on p. 15).

[28] Z. Zhang et al. "Magnetic shielding properties of GdBCO bulks with different crystal orientation". In: *Physics Procedia* 27 (2012). Proceedings of the 24th International Symposium on Superconductivity (ISS 2011), October 24-26, 2011, Tokyo, Japan, pp. 180–183. ISSN: 1875-3892. DOI: https://doi.org/10.1016/j.phpro.2012.03.440. URL: https://www.sciencedirect.com/science/article/pii/S1875389212008565 (cit. on p. 15).

[29] F. M. F. S. do Vale. "Desenvolvimento de um dispositivo de medida para determinação dos esforços eletromecânicos em limitadores de corrente supercondutores". In: *MA thesis* (2019). DOI: http://hdl.handle.net/10362/115837 (cit. on p. 28).

I

Annex

This chapter contains the file used for 3D printing the new mold that fixates the secondary windings, taken from [7].

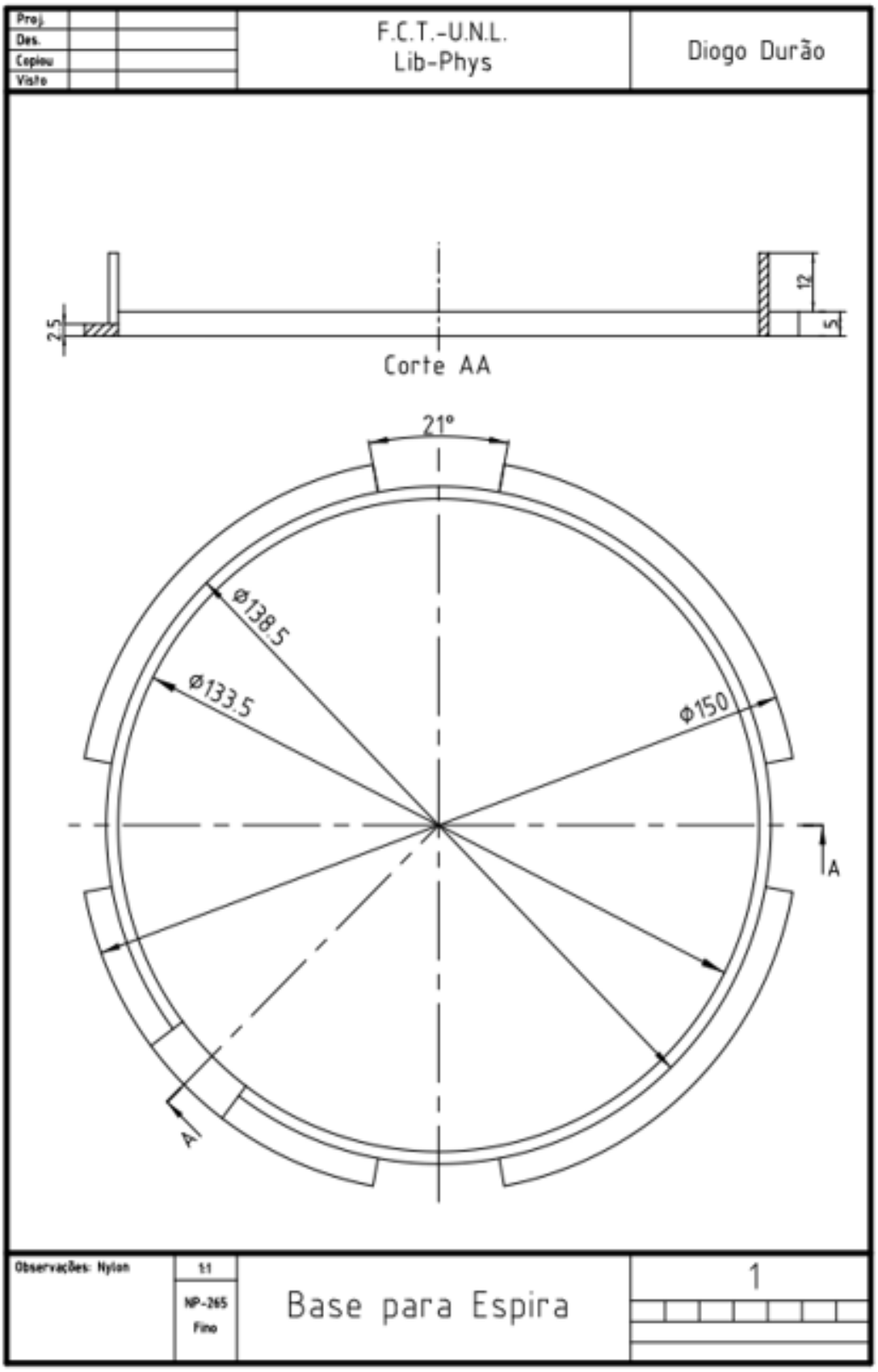

Figure I.1: Schematic of the mold used for the winding samples.